Formation of continental microplates through rift linkage: Numerical modelling and its application to the Flemish Cap and Sao Paulo Plateau

Derek Neuharth[1,2], Sascha Brune[1,2], Anne Glerum[1], Christian Heine[3], J. Kim Welford[4]

[1]GFZ German Research Centre for Geosciences, Potsdam, Germany.

[2]Institute of Geosciences, University of Potsdam, Germany.

[3]Specialist Geosciences, PTD/E/F, Shell Global Solutions International B.V., Rijswijk, NL

[4]Department of Earth Sciences, Memorial University of Newfoundland, St. John's, Newfoundland, Canada

Corresponding author: Derek Neuharth (djneuh@gfz-potsdam.de)

Key Points:

- Strike-perpendicular offset and crustal strength control the mode of rift segment linkage (microplate, oblique, or transform).
- Rotating continental microplates form at offsets of >200 km for weak and moderately strong crust.
- Modelled microplate evolution may explain the formation of the Flemish Cap, the Sao Paulo Plateau and other continental promontories.

Abstract

Continental microplates are enigmatic plate boundary features, which can occur in extensional and compressional regimes. Here we focus on microplate formation and their temporal evolution in continental rift settings. To this aim, we employ the geodynamic finite element software ASPECT to conduct 3D lithospheric-scale numerical models from rift inception to continental breakup. We find that depending on the strike-perpendicular offset and crustal strength, rift segments connect or interact through one of four regimes: (1) an oblique rift, (2) a transform fault, (3) a rotating continental microplate or (4) a rift jump. We highlight that rotating microplates form at offsets >200 km in weak to moderately strong crustal setups. We describe the dynamics of microplate evolution from initial rift propagation, to segment overlap, vertical-axis rotation, and eventually continental breakup. These models may explain microplate size and kinematics of the Flemish Cap, the Sao Paulo Plateau and other continental microplates that formed during continental rifting worldwide.

Plain language summary

Microplates are enigmatic features that form in the boundaries between tectonic plates. In continental rifts, plates are successively broken to eventually form new oceans. As the continental crust is very heterogeneous, rifts rarely form in straight lines. In some cases, individual rift segments initiate hundreds of kilometers apart both along and perpendicular to strike and as these segments grow, they interact and link. Here we use 3D computer simulations to investigate the linkage of offset rifts. We find that rift linkage is primarily contolled by the strike-perpendicular offset and crustal strength. At low offset they link through an oblique rift segment, at medium offset a transform fault is formed, and at large offsets in weak crust they overlap and rotate a central block known as a microplate. We suggest that the latter processes has shaped the Flemish Cap, the Sao Paulo Plateau, and many other continental promontories at rifted margins worldwide.

1 Introduction

Microplates have been identified in extensional (e.g., Danakil microplate; Eagles et al., 2002) and compressional regimes (e.g., Tibet microplate; Thatcher, 2007). Contrary to the common picture of large, rigid, tectonic plates surrounded by weak and narrow plate boundaries, microplates exist at an intermediate scale: they are larger than the fault blocks that make up the narrow plate boundaries, yet smaller and rotate on a different axis than the surrounding tectonic plates (Macdonald et al., 1991; Schouten et al., 1993). While previous explanations for extensional microplates have been based on analogue models (e.g., Dubinin et al., 2018; Katz et al., 2005) or 2D concepts (Müller et al., 2001; Péron-Pinvidic & Manatschal, 2010), the impact of 3D continental rift dynamics, so far, remains unclear.

In this study, we use 3D models to test the hypothesis that extensional microplates form due to offset rift segments. Rift segments may form at an offset due to, for example, along-strike variability that can be caused by inherited weaknesses (Heine et al., 2013; de Wit et al., 2008) or along-strike changes in rheological structure (Brune et al., 2017a; Corti et al., 2019). Eventually, these variabilities may lead to offset rift propagation from opposite directions. Examples of

offset rift systems exist along rifted margins, such as in the South Atlantic (Heine et al., 2013), the Jan Mayen microcontinent in the Norwegian-Greenland Sea (Gernigon et al., 2012), and in the present-day East African and Red Sea Rift System (Calais et al., 2006; Eagles et al., 2002; Stamps et al., 2008; Stamps et al., 2021). The strike-perpendicular offset is likely an important factor in how rift segments eventually link, and the structural features that form in response (Allken et al., 2012; Gerya, 2013a). Based on present-day mid-ocean ridges, it has been shown that offset divergent segments can connect through long transform faults, or, in some cases, interacting ridges overlap and rotate a central microplate located between the two ridges (Macdonald et al., 1991).

Oceanic microplates are tectonic features that form between adjacent extensional zones (e.g., the Easter microplate located at the East Pacific Rise; Naar & Hey, 1991). When two offset spreading centers interact, they create drag forces along the edges of the rigid microplate that exists in the overlapping zone (Katz et al., 2005; Schouten et al., 1993). These drag forces rotate the microplate about a vertical axis. The microplate rotation speed increases with the extensional velocity and decreases with the size of the microplate (Schouten et al., 1993). In oceanic crust, overlapping spreading centers have small offsets (2-30 km; Macdonald et al., 1991) and form fast-rotating (~10°/Myr; Naar & Hey, 1991) short-lived (5-10 Myr; Keary et al., 2009) microplates that attach to one margin as a single spreading center becomes dominant.

Microplates can form in continental crust between overlapping offset rifts. The offset needed for microplate formation is related to the thickness of the brittle layer in the lithosphere (Vendeville & Le Calvez, 1995), which is significantly larger in incipient rifts than in proximity of mid-oceanic spreading centres. Thus continental microplates are likely larger and slower than oceanic ones. For example, in East Africa two rift branches guided by preexisting weak suture zones overlap and rotate the Victoria microplate by ~0.07°/Myr (Glerum et al., 2020). Evidence for remnant continental microplates exists along passive margins, where seismic data suggest thinned crust surrounding regions of relatively thick continental crust (e.g., the Flemish Cap; Welford et al., 2012) or magmatic crust which may contain some mixture of continental crust (e.g., Sao Paulo Plateau; Scotchman et al., 2010).

Other continental promontories that likely formed as microplates via overlapping rift segments can be found in the Atlantic Ocean: the Galicia Bank, Porcupine Bank, Rockall Bank offshore Western Europe, and the Faroes/Fugloy ridge North of Scotland (King et al., 2020; Peace et al., 2019; Scotchman et al., 2010; Yang & Welford, 2021), the NE Brazilian Sergipe Microplate that is bordered by the failed Tucano and Jatoba Rifts (Heine et al., 2013; Szatmari & Milani, 1999), as well as the Falkland Islands microcontinent (Stanca et al., 2019). A prominent example in the Indian Ocean is Sri Lanka (Gibbons et al., 2013; Premarathne et al., 2016), and a perhaps less obvious one is the Exmouth Plateau on the Australian NW Shelf which operated briefly in the late Jurassic (Heine & Müller, 2005; Longley et al., 2002). Despite ample evidence of actively rotating and remnant continental microplates, there is only scarce observational data to constrain the evolution of a continental microplate from initial fault propagation to overlapping rift arms and rotation, and eventually, to continental-breakup and seafloor spreading.

In this study, we use numerical modelling to elucidate when continental microplates form, how they evolve, and how modelled microplates compare to real world examples. We perform 3D extensional simulations where we vary key parameters such as the along-strike and strike-perpendicular offsets of the initial rift segments, the crustal strength, and the lithosphere

thickness (Fig. 1). The models are extended for 25 Myr, often past continental breakup, and allow us to characterize the general types of rift linkage and to assess how these connections vary through our parameter space. Finally, we compare a representative model to two possible microplates, the Flemish Cap and Sao Paulo Plateau, located in the North and South Atlantic, respectively. Our models reveal similarities in the general geometry (e.g., microplate size and crustal thickness patterns) and the mechanisms involved in its formation.

2 Methods

2.1 Governing equations

We perform numerical simulations of a 3D extensional system using the open source finite-element code ASPECT (Advanced Solver for Problems in Earth's ConvecTion, version 2.1.0; Heister et al., 2017; Kronbichler et al., 2012; Rose et al., 2017; Bangerth et al., 2019). While this software was originally developed to study global mantle convection, it has successfully been adopted to model geodynamic processes of lithosphere deformation (Heckenbach et al., 2021; Heron et al., 2019; Muluneh et al., 2020; Naliboff et al., 2020; Sandiford et al., 2021). ASPECT solves the following extended Boussinesq conservation equations assuming an infinite Prandtl number (i.e. without the inertial term),

$$-\nabla \cdot (2\eta\dot{\varepsilon}) + \nabla P = \rho \boldsymbol{g}, \tag{1}$$

$$\nabla \cdot (\boldsymbol{u}) = 0, \tag{2}$$

$$\bar{\rho} C_p \left(\frac{\partial T}{\partial t} + \boldsymbol{u} \cdot \nabla T\right) - \nabla \cdot k \nabla T = \bar{\rho} H + (2\eta\dot{\varepsilon}) : \dot{\varepsilon} + \alpha T (\boldsymbol{u} \cdot \nabla P), \tag{3}$$

$$\frac{\partial c_i}{\partial t} + \boldsymbol{u} \cdot \nabla c_i = q_i \tag{4}$$

where equation (1) represents the conservation of momentum, with η the effective viscosity, $\dot{\varepsilon}$ the deviator of the strain rate tensor (defined as $\frac{1}{2}(\nabla \boldsymbol{u} + (\nabla \boldsymbol{u})^{\mathrm{T}})$), $\boldsymbol{u}$ the velocity, P the pressure, ρ the density, and $\boldsymbol{g}$ gravity. Equation (2) describes the conservation of volume. Equation (3) represents the conservation of energy where $\bar{\rho}$ is the reference adiabatic density, C_p the specific heat capacity, T the temperature, k the thermal conductivity, H the radiogenic heating, and α the thermal expansivity. As right-hand-side heating terms, we include radioactive heating, frictional heating, and adiabatic heating from top to bottom, respectively. Finally, we solve the advection equation (4) for each compositional field c_i (e.g., upper crust, lower crust, and accumulated plastic strain) with nonzero reaction rate q_i only for the plastic strain field.

2.1.1 Rheology

We use a viscoplastic rheology (Glerum et al., 2018), which additionally includes plastic weakening based on accumulated plastic strain. In the viscous regime, we use a composite of diffusion and dislocation creep (Karato & Wu, 1993), formulated as:

$$\eta_{eff}^{diff|dis} = \frac{1}{2} A_{diff|dis}^{\frac{-1}{n}} d^{m} \dot{\varepsilon}_{e}^{\frac{1-n}{n}} \exp\left(\frac{\left(E_{diff|dis} + PV_{diff|dis}\right)}{nRT}\right), \tag{5}$$

where A is a scalar prefactor, d the grain size, $\dot{\varepsilon}_e$ the square root of second invariant of the deviatoric strain rate, E the activation energy, P the pressure, V the activation volume, R the gas constant, T the temperature, and n the stress exponent. For diffusion, n = 1 and the equation becomes independent of strain rate. For dislocation creep, the grain size exponent m vanishes, rendering dislocation creep independent of grain size. Values for A, E, V, and n used in our models are composition-dependent and found in supplementary Table S1.

In the plastic regime, when viscous stresses exceed the yield stress, we use the Drucker-Prager yield criterion (Davis & Selvadurai, 2002). The effective plastic viscosity is given by

$$\eta_{eff}^{pl} = \frac{\frac{6C\cos\phi}{\sqrt{3}(3-sin\phi)} + \frac{6P\,sin\phi}{\sqrt{3}(3-sin\phi)}}{2\dot{\varepsilon}_e}, \quad (6)$$

where C is the cohesion and ϕ the internal angle of friction. The accumulation of plastic strain is tracked as a compositional field. This field is used to linearly weaken ϕ from an initial value of 26.56° (friction coefficient of 0.5) to a final value of 2.656° (friction coefficient of 0.05) over the

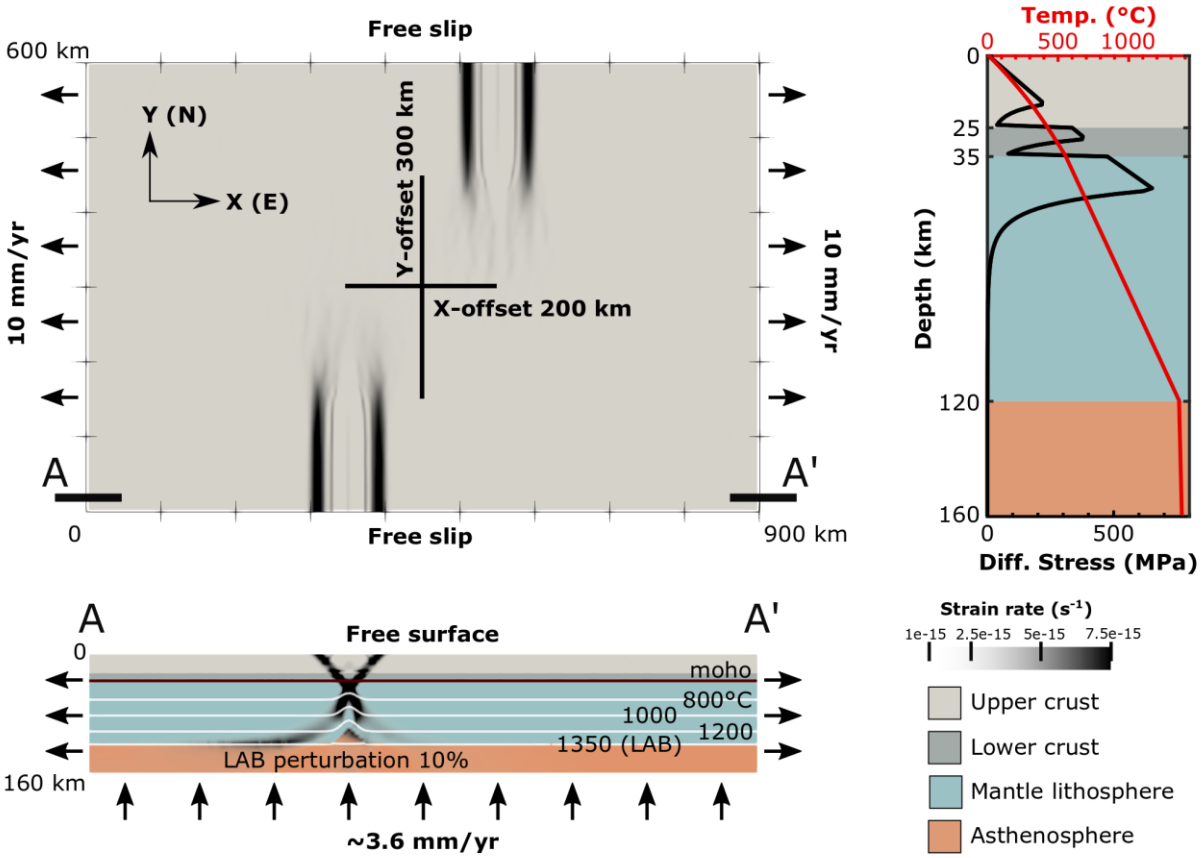

Figure 1: Reference model setup for a Y-offset of 300 km and an X-offset of 200 km, depicted at 0 Myr model time. A vertical slice at 0 Myr is included to show the initial strain that localizes above the thermal/compositional LAB perturbation. A strength profile shows a temperature (red) and strength (black) profile, and the unperturbed compositional depths. The yield strength profile is computed using a reference strain rate of 7.05e-16 1/s, the initial bulk strain rate. Density profile given in supplementary Fig. S1.

accumulated plastic strain interval of 0 to 1. The time-integrated value of the strain reaction rate q_i is approximated as $\dot{\varepsilon}_e \cdot dt$ when plastic yielding occurs (with dt the timestep size).

2.2 Model setup

In this study we examine how the initial placement of two rift arms affects their connection. We therefore set up a 3D box model with dimensions 900x600x160 km (X, Y, and Z, where Z is depth) and 4 compositions representing a wet quartzite upper crust (Rutter & Brodie, 2004), wet anorthite lower crust (Rybacki et al., 2006), and dry olivine lithospheric mantle and asthenosphere (Hirth & Kohlstedt, 2003; Fig. 1). The total crustal thickness is set to 35 km, with the reference models using a ratio of 25 km upper to 10 km lower crust, a crustal configuration that is representative of typical continental interiors (Mooney, 2010; Pasyanos et al., 2014). This ratio is varied when testing the crustal strength. The lithospheric mantle extends between the crust and the lithosphere-asthenosphere boundary (LAB) at 120 km depth. The LAB depth represents a typical, i.e. non-cratonic, non-orogenic, intracontinental setting (Artemieva, 2006; Pasyanos et al., 2014). The remaining material beneath the LAB is considered asthenosphere.

The model mesh consists of 3 different levels of resolution based on model depth. The maximum resolution of 5 km extends from the surface to 50 km depth, where the transition from plastic to viscous yielding in the mantle lithosphere generally occurs. This allows us to resolve all plastically deforming material at the highest resolution. Lower resolved 10-km mesh cells are then used until 80 km depth, and below that the remaining lithospheric mantle and asthenosphere are resolved at 20 km.

The initial temperature above the LAB is determined by a steady-state geotherm (Turcotte & Schubert, 2002), and below by a mantle adiabat. For simplicity, the initial rift arms are seeded through a small perturbation: we raise the LAB locally by 10% of the lithospheric thickness. We fix the top boundary temperature at 0 °C, and the bottom boundary at the temperature initially determined from the mantle adiabat. All other boundaries are set to zero heat-flux.

Mechanically, the model is extended for 25 Myr at a velocity of 20 mm/yr giving a total extension of 500 km. This involves prescribed outflow of 10 mm/yr on the east and west boundaries, with inflow through the bottom boundary to conserve volume. The north and south boundaries are set to free slip, and the top boundary is a true free surface.

Although our model captures some of the complexity involved in rift systems, we note that there are several processes which likely affect rift evolution that are not included. For instance, in the models presented here we assume deformation initially localizes above seeded LAB perturbations, however in nature this localization may instead be related to plume activity (Buiter & Torsvik, 2014; Koptev et al., 2018). Additionally, while the lithosphere thickness varies spatially (Artemieva & Mooney, 2001; Artemieva, 2006; Koptev & Ershov, 2011) and likely includes heterogeneities, our models are spatially homogeneous and we do not consider how crustal or lithospheric-scale inheritance may affect the results (e.g. mantle scarring; Heron et al., 2019). Also, we do not consider the movement and deposition of sediment through surface processes. Finally, magmatic processes such as the thermal effect of melt and its movement (e.g., diking and underplating) are not considered, which may result in less drastic weakening (Bahadori & Holt, 2019; Gerya et al, 2015).

3 Generic models

In this section, we investigate and discuss the connection between offset rift arms through a series of 48 numerical extension models. We vary 4 parameters to test their effect on rift connection: (1) the offset of pre-defined rift arms perpendicular to the rift trend, i.e. in the X-direction (Fig. 2 to 5); (2) their offset along-strike, i.e. in the Y-direction (Fig. 6); (3) the crustal strength (Fig. 7); and (4) the lithosphere thickness (supplementary Fig. S3). Offset in the X-direction is varied from a small initial offset of 100 km up to 400 km, where offset rifts no longer interact (Le Pourhiet et al., 2017). The Y-offset is similarly varied between 100 km and 400 km, always including some positive offset (underlap) to let overlap develop naturally while testing whether the time-dependency of along-strike rift offset directly affects the resulting connection. We vary the crustal strength by changing the crustal ratio of upper to lower crust from 35:0 to 10:25 km to span the range of possible crustal configurations (Mooney, 2010). Finally, the lithosphere thickness is varied between 80 and 140 km.

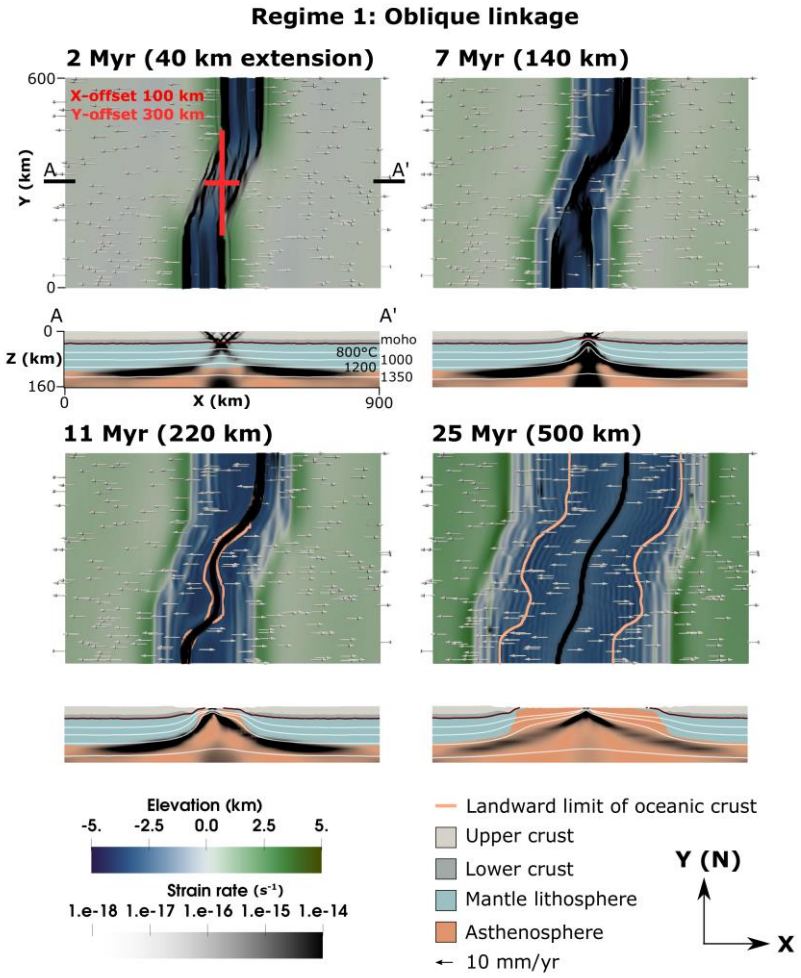

Figure 2: Evolution of the oblique linkage in Regime 1. The top down view shows the elevation (green to blue), the strain rate (transparent to black), and the landward limit of oceanic crust (>70% mantle material, orange line). Velocity arrows indicating the horizontal velocity are scaled with the velocity magnitude. Slices show the profile from A to A' in the X-direction (supplementary video S1). Dark red line shows a contour of the Moho, and white lines temperature contours.

3.1 X-offset results

We run four model simulations with X-offsets of 100, 200, 300, and 400 km. The Y-offset is kept at 300 km and the ratio of upper to lower crust at 25:10 km. In these cases, each change in the X-offset results in a different type of connection, or lack thereof, between the rift arms, and we distinguish 4 different kinematic regimes: *Regime 1*: connection through an oblique rift (Fig. 2); *Regime 2*: connection through a transform fault (Fig. 3); *Regime 3*: formation of a continental microplate followed by an eventual rift jump (Fig. 4); and *Regime 4*: rift jump with no interaction between the rifts (Fig. 5).

3.1.1 *Regime 1*: oblique linkage

Two rift arms are emplaced 100 km apart in the X-direction and strain localizes on two initial faults at a dip angle of ~45° above the perturbation (see Fig. 2 and supplementary video S1). By 2 Myr, a ~3.7 km deep rift valley forms between the initial faults on both sides and strain begins to localize in the center of these valleys. Simultaneously, rift tips propagate into the undeformed crust establishing multiple oblique (azimuth angle of ~25°) faults which bridge the two deeper rift valleys through a ~2 km deep depression (Heidbach et al., 2007) in the center. Deformation

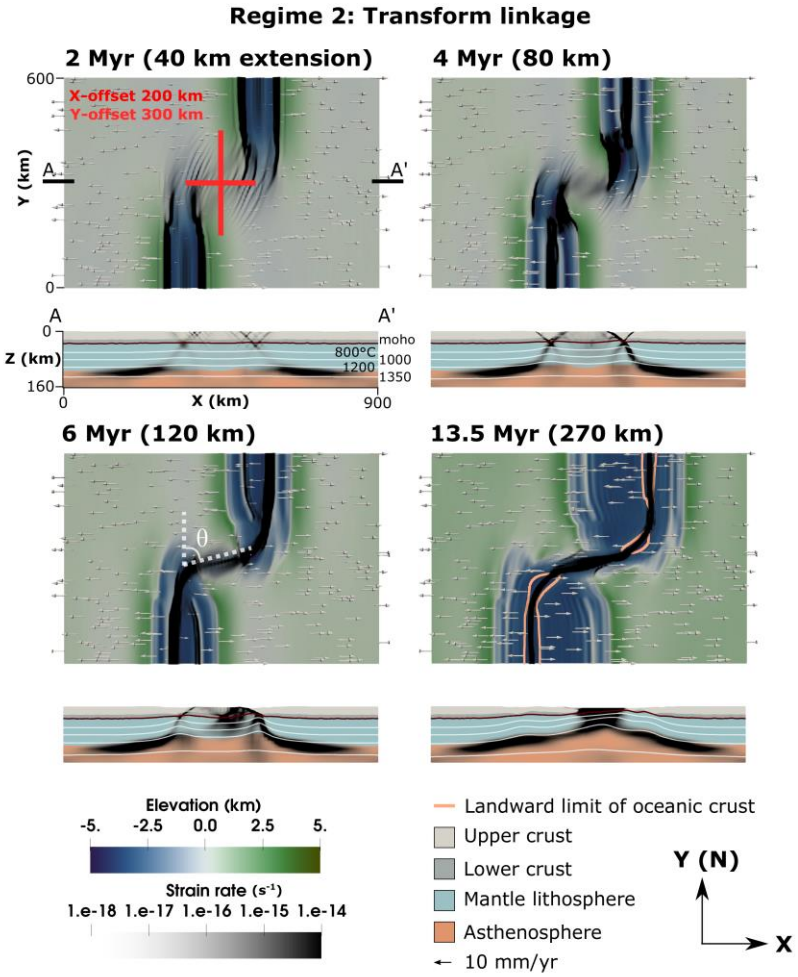

Figure 3: Evolution of the transform fault connecting the rifts in *Regime 2* (supplementary video S2), where θ represents the linkage angle. Refer to Fig. 2 for explanation.

transfers from these oblique faults into the center of the rift valley, and by 4.5 Myr the two arms fully connect across the model domain. At this time, a single ~22°-striking oblique fault becomes dominant in the center, while in the north and south deformation continues on two faults which remain orthogonal to extension. As extension continues, rift migration begins and small differences from numerical noise lead to along-strike changes in the migration direction for the central and southern rift segments (Fig. 2, 7 Myr). This migration phase ends earlier in the central segment, causing the onset of crustal breakup. By 11 Myr the faults have stabilized and form a continuous fault zone with a general obliquity of ~20° as seafloor spreading begins.

3.1.2 *Regime 2*: transform linkage

The initial distance between the rift arms is increased to 200 km in the X-direction, and strain initiates two faults (Fig. 3, supplementary video S2) similar to the previous model. By 2 Myr, the rift tips propagate into the undeformed crust, curving inward toward the opposite rift arm at an ~24° azimuth angle. At 4 Myr, strain localizes in the rift valley of each rift arm, and the initial faults cease to be active. At 6 Myr these new faults link through the topographically high center by a ~75°-striking oblique fault that forms within an oblique necking zone between the offset rift

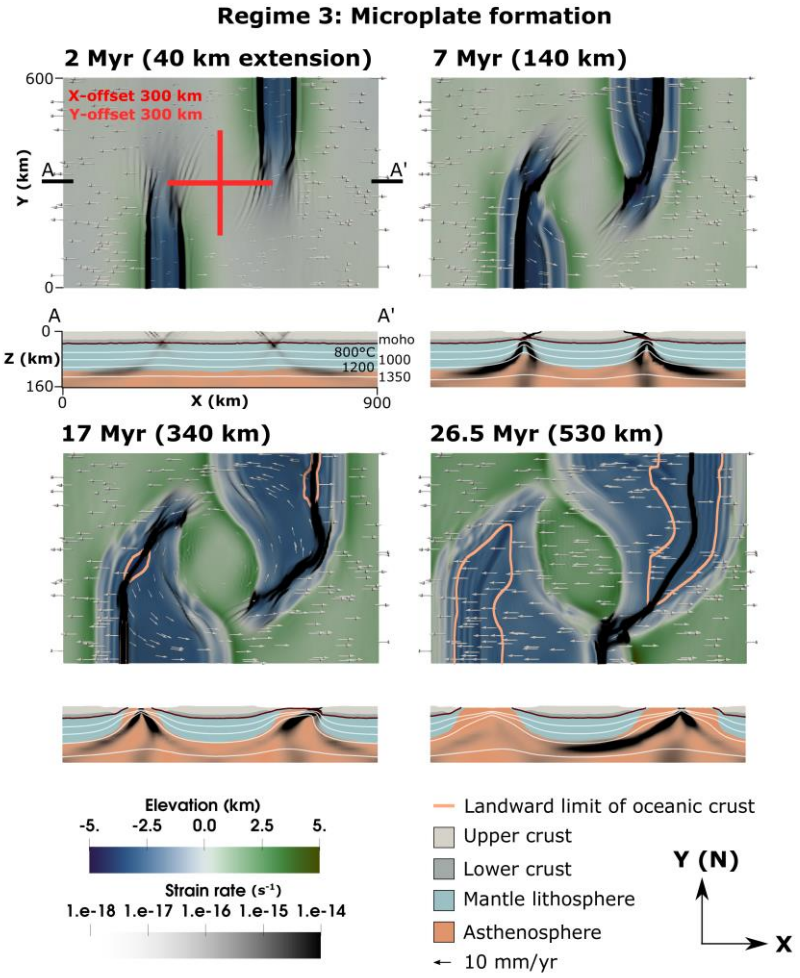

Figure 4: Evolution showing the formation and rotation of the microplate seen in *Regime 3* (supplementary video S3). Refer to Fig. 2 for explanation.

arms. The northern and southern rift arms migrate towards the east and west model boundaries, respectively, until 13.5 Myr, when migration stops and seafloor spreading begins. Like in Le Pourhiet et al. (2017), our models reproduce the process of steady-state rift migration and the generation of wide stretches of hyperextended crust (Brune et al., 2014, 2017b; Pérez-Gussinyé et al., 2020; Svartman Dias et al., 2015; Tetreault & Buiter, 2018). As strain further localizes, a short ~100 km transform fault forms, through continental crust, within the highly oblique fault that connects the two rift arms.

3.1.3 *Regime 3*: microplate formation

The X-offset of the rift arms is further increased to 300 km, and the rift tips initially propagate forward into the undeformed crust (Fig. 4, supplementary video S3). At 2 Myr the tips overlap ~230 km and curve inward at a 20° azimuth angle. Deformation in both rifts localizes in the rift valley forming a center fault. By 7 Myr, the center faults remain generally orthogonal to extension, except the tips which curve inward. As extension continues, the rifts migrate outward to the east and west. Overlap between the rift arms increases as the rift tips, unable to connect through the topographically high center block, propagate forward developing into two sections: an orthogonal section near the model north and south boundaries and 50°-striking (east) and 35°-

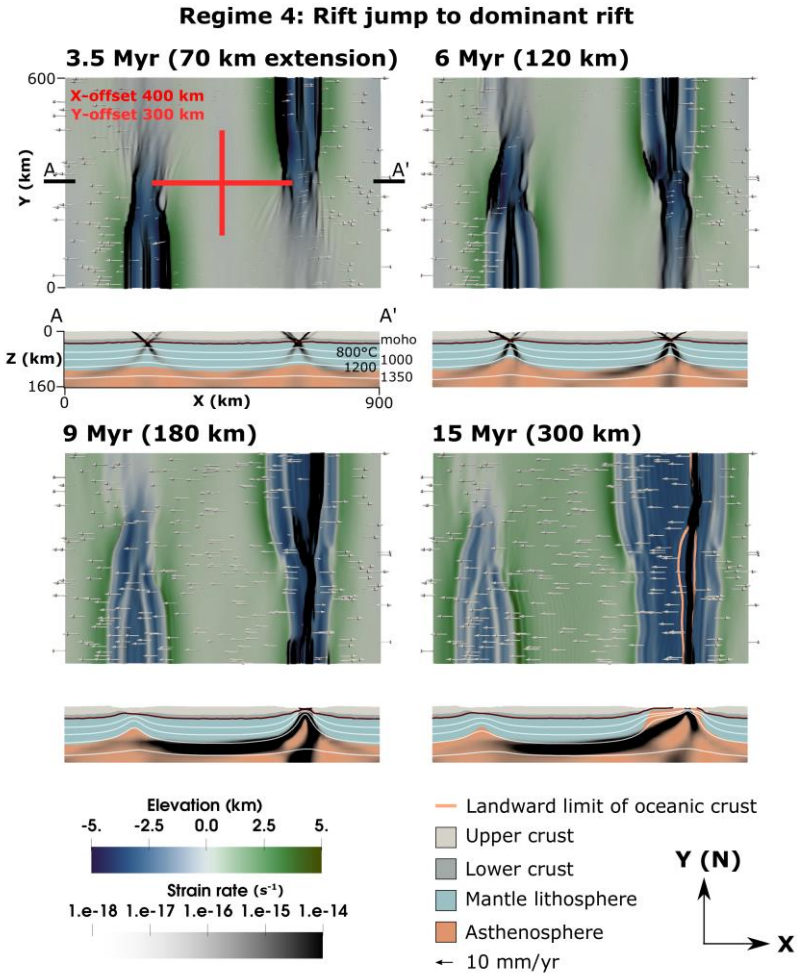

Figure 5: Evolution of the rift jump seen in *Regime 4* (supplementary video S4). Refer to Fig. 2 for explanation.

striking (west) oblique sections where the rift arms overlap. Simultaneously, extension causes uplift and counterclockwise rotation of the relatively undeformed center between the overlapping, right-stepping rifts, thus creating a rigid, independently rotating, continental microplate. By 17 Myr, seafloor spreading has begun on both rift arms. Microplate rotation continues as the rifts migrate east-west and propagate north-south, until ~25 Myr when the eastern rift arm reaches the southern boundary, attaching the microplate to the western side. Subsequently, the western rift delocalizes and then fully dies out by 26.5 Myr, leaving a ~240 km wide-uplifted microplate core (measured in the X-direction along the center).

3.1.4 *Regime 4*: rift jump to dominant rift

Rift arms are initially emplaced 400 km apart in the X-direction (Fig. 5, supplementary video S4). Initial faults diffusely propagate forward into undeformed crust in the Y-direction, before secondary border faults form, slightly inward, but parallel to the initial ones. At 3.5 Myr, strain begins to localize in the rift valley between the initial faults, establishing a center fault. Simultaneously, the secondary faults continue to propagate through the crust in the Y-direction. By 6 Myr the initial faults are inactive, and the center fault links to one of the secondary faults, which in the case of the eastern rift extend to the southern boundary. In the eastern rift, the center fault propagates along the western secondary border fault localizing in the rift valley created by the two secondary faults. At 9 Myr, the western rift has completely died out while the eastern rift's center fault has crossed the entire model domain. The eastern rift migrates eastward until 15 Myr. At this time, rift migration ceases as seafloor spreading begins.

3.1.5 X-offset interpretation

The changes in regime with increasing X-offset suggest that X-offset exerts a major control on rift linkage dynamics. Small offsets allow rifts to easily interact and connect through an oblique fault (*Regime 1*). By increasing the offset, the rifts propagate farther forward before connecting. This suggests that, as offset increases, the connecting rift will become more oblique (i.e. higher linkage angle, see θ in Fig. 3) until obliquity is high enough to connect the rifts through a transform fault (*Regime 2*). As the offset is further increased (>200 km), the rifts interact but cannot link through the strong continental block between the two rift arms. This leads to further overlap and center block rotation as the faults co-exist, forming a microplate that rotates until an eventual rift jump to the dominant rift. Further increasing the X-offset likely decreases the interaction between the two rifts, lowering the amount of microplate rotation. Eventually, at 400 km, the rifts are too far apart to interact before reaching the opposite model boundary. While in nature at some X-offset rifts should no longer interact, analogue models suggest that the formation of overlapping spreading centers becomes more likely as rift segment length increases relative to the offset (Acocella, 2008). Thus, it is likely that in our models regime 4 is affected by our boundary conditions. To test this, we ran an additional simulation where the length of the model in the Y-direction was increased to 900 km. Indeed, in this case, the rifts interact and a comparably large microplate forms (supplementary Fig. S2) suggesting that there is no upper limit for the size of a microplate in our model setup.

3.2 Y-offset results

In nature, the along-strike offset of two rift arms is a function of time; rifts that propagate along-strike will initially have a large Y-offset that gradually shrinks. Therefore, we expect that the initial Y-offset does not have a large impact on the type of connection. To test this, we perform a

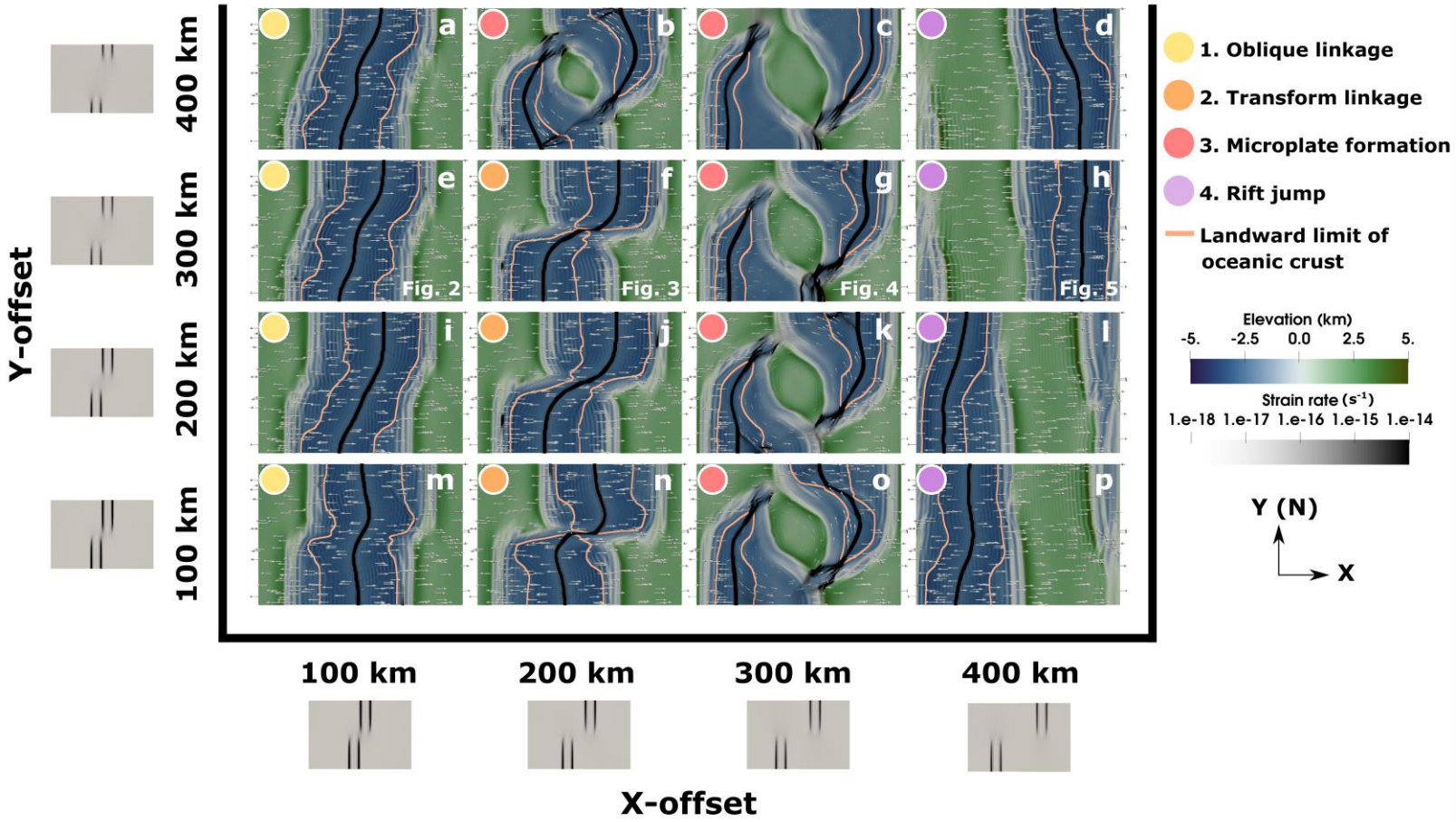

Figure 6: Regime diagram showing the types of rift connections seen when varying the initial X- and Y-offset. Models are shown from a top down view at 25 Myr, and are colored by elevation and the strain rate, with the orange line representing the landward limit of oceanic crust (>70% asthenosphere material). Models are divided into regimes shown with colored dots in the top-left corners of the model images.

1

series of models varying the Y-offsets from 100 km to 400 km for each of the previously employed X-offsets, the results of which are shown in Fig. 6. Indeed, in almost all cases, the Y-offset did not impact the connection type. This suggests that the time-dependency of the Y-offset does not lead to a certain regime dominating, but rather the rift's X-offset when they are close enough to interact controls the subsequent connection. There is some variation in the connection at X-offsets of 200 km. This may relate to a 200-km X-offset being a transitional length between *Regimes 2* and *3*.

3.3 Crustal strength results

To investigate the role crustal strength plays in the connection of offset rifts, we varied the ratios of upper to lower crust between 35:0 (weak), 25:10, 20:15, 15:20, and 10:25 km (strong, see Fig. 7). Otherwise the model setups remain identical to the reference models (Fig. 2 to 5). Figure 7 suggests that crustal strength is an important factor in determining how offset rifts link. In this model setup, a higher crustal strength relates to a higher ratio of plastic to viscous deforming material, which results in greater plastic strain localization. As strain becomes more localized, faults connect rather than diffusely propagating forward, resulting in less overlap as crustal strength increases. Thus, at higher crustal strength, larger initial offsets are needed to form transform faults, and microplates do not form as faults connect instead of overlap.

3.4 Lithosphere thickness results

To assess the impact of initial lithosphere thickness on rift linkage, we varied the lithosphere thickness from 80 to 140 km (supplementary Fig. S3). The setup of these models is similar to those shown in Fig. 6e-h, with a crustal ratio of 25:10, Y-offset of 300 km, and variable X-offset between 100 and 400 km, although with a larger Z-extent of 280 km. The resulting regime diagram after 25 Myr is very similar to the model suite where we varied crustal strength (Fig. 7), with thicker, colder lithosphere leading to enhanced plastic strain localization similar to having a thicker layer of strong lower crust. Again, the distribution of regimes is largely determined by the X-offset. In contrast to our previous results however, the deformation does not localize in distinct rift segments if the initial lithosphere thickness is smaller than 80 km. In these cases, lithospheric strength is so low that the initial, 10 km thick LAB perturbation that seeds the rift segments is not sufficient in driving rift localization.

3.5 Discussion and comparison to previous work

Our study suggests that offset rifts link through four different regimes, which are dependent on the X-offset of the rift arms and the crustal strength. Our results and connection types are similar to what is seen in earlier analogue and numerical experiments, where models connect through transfer zones leading to oblique (like *Regime 1*) or transform fault (*Regime 2*) connections, or by accommodation zones where overlapping spreading centers, which can be considered precursors to microplate development, form (*Regime 3*, Acocella, 2008; Allken et al., 2011, 2012; Gerya, 2013b; Le Pourhiet et al., 2017; Tentler, 2003; Tentler & Acocella, 2010; Zwaan et al., 2016). Similarly, at large offsets, no rift connection occurs (*Regime 4*, Allken et al., 2011, 2012; Le Calvez & Vendeville, 2002; Le Pourhiet et al., 2017). However, in many of these previous models smaller initial X-offsets were used (~50-120 km), and in contrast to our study differences were seen when varying the Y-offset (e.g., Tentler & Acocella, 2010).

43

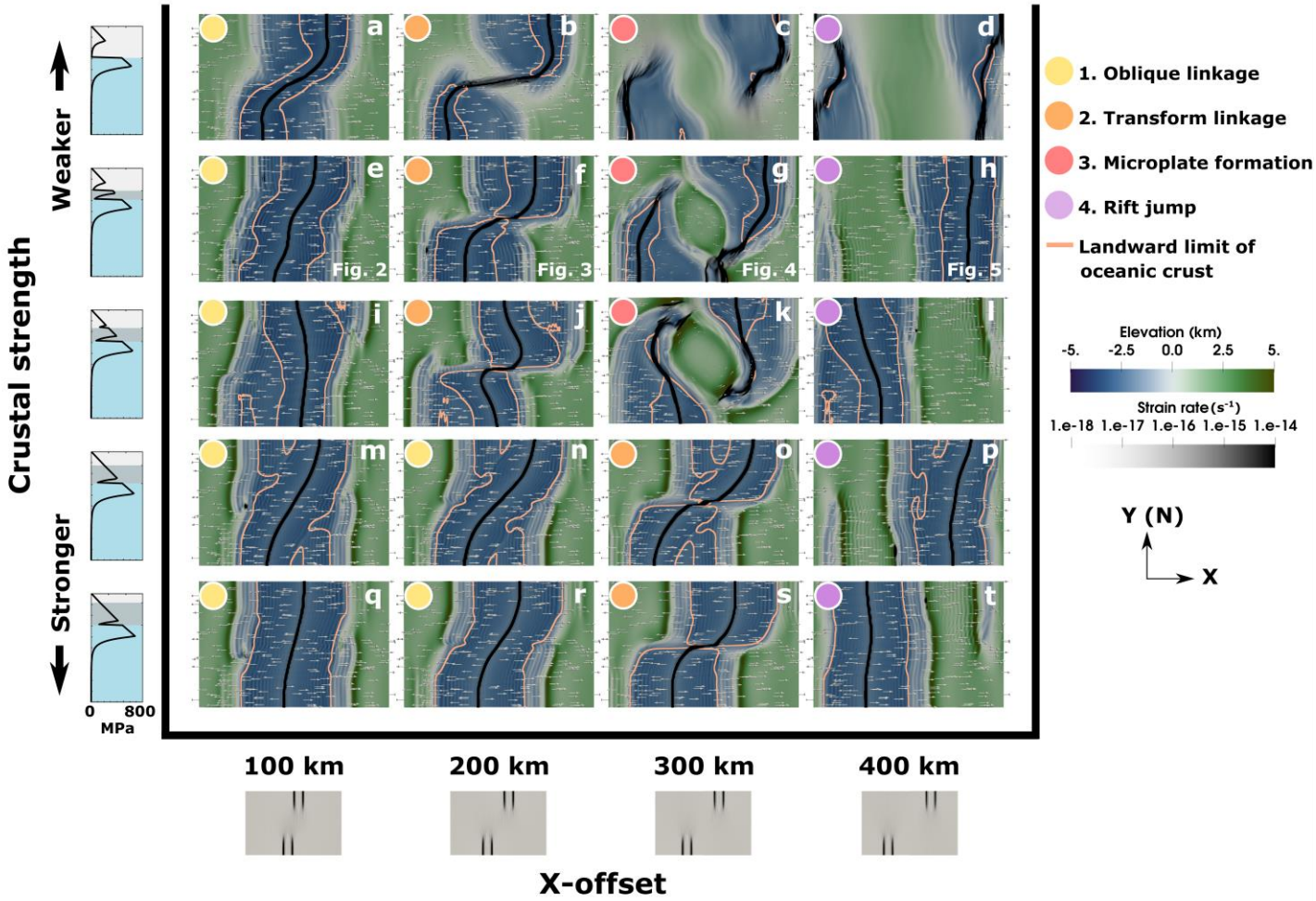

Figure 7: Regime diagram showing the types of rift connections when varying the ratio of upper to lower crust, and the initial x- offset. Models are shown from a top down view at 25 Myr, and are colored by elevation and the strain rate, with the orange line representing the landward limit of oceanic crust (>70% asthenosphere material). On the left, strength envelopes are shown, with the compositions of upper (light gray) and lower (dark gray) crust, and mantle lithosphere (blue). Models are divided into regimes shown with colored dots in the top-left corners of the model images.

An important factor in the mode of rift linkage is the linkage angle (with 90° being strike-perpendicular, see θ in Fig. 3). In previous analogue modelling studies, the linkage angle was found to be a function of the Y-offset, with the angle increasing as Y-offset was reduced (Tentler & Acocella, 2010). Mechanically, most aforementioned analogue setups involve a brittle layer overlying a viscous material. This setup strongly resembles our models with a crustal ratio of 10:25 km (Fig. 7q-t) where nearly the entire crustal region acts as a single brittle block. While we varied the Y-offset in a weaker crustal setup, we found that Y-offset has little effect on overall connection type, which is instead dependent on the X-offset. Similarly, in our reference setup we find that linkage angles increase with the X-offset and not the Y-offset. In addition, Le Pourhiet et al., (2017) suggest that the linkage angle is also a function of crustal strength, and that linkage angles decrease in strong crust. Our findings agree with this (Fig. 7, see also supplementary animations), and additionally suggest that the control of the X-offset on rift linkage angles becomes less obvious in strong rheologies. We suggest that due to greater plastic strain localization in stronger crust rift linkage becomes more efficient, thus rifts are likely to link at larger Y-offsets than in weak crust leading to lower linkage angles.

Although we find that overall crustal strength contributes to the style of rift linkage, our models corroborate earlier findings that the integrated brittle strength plays an even more important role. Using crustal-scale models with a brittle upper crust overlying a ductile lower crust, Allken et al. (2011, 2012) suggest that less cohesion and plastic strain weakening favors diffuse rift propagation and overlap. Similarly, we show that models less susceptible to plastic strain weakening (i.e., a lower ratio of brittle to ductile deforming material) have more diffuse rift propagation. In addition, we find that in models with greater integrated brittle strength, rifts are more susceptible to plastic weakening. This generates focused rifts that are likely to connect earlier at lower linkage angles and thus less likely to overlap. If however the integrated brittle strength is lower and localization less effective, rifts propagate more diffusely allowing higher linkage angles and increasing the likelihood of overlap and continental microplate formation. These results suggest that overall crustal strength is less important to the style of rift linkage than the integrated brittle strength. This finding is similar to that of Naliboff and Buiter (2015), who suggested that integrated brittle strength exerts key control on rift reactivation

An additional factor governing linkage kinematics is rift propagation speed (Jourdon et al., 2020; Le Pourhiet et al., 2018). When propagation is slow, deformation becomes more diffuse. Shortening parallel to the rift propagation direction reduces the rift propagation speed resulting in diffuse V-shaped rift propagation (Le Pourhiet et al., 2018). In our models, where rifts overlap rotation occurs in the overlapping region, and this rotation applies a shortening component to the rift tips (Fig. 4, 17 Myr), slowing rift propagation. For *Regime 2*, the overlapping region is small and deformation quickly localizes into strike-slip motion. However, for *Regime 3*, where the rifts cannot easily link, rotation continues to apply shortening to the rift tips prolonging microplate rotation and leading to V-shaped propagation on both sides of the microplate. Figure 7 suggests that microplates form in a small crustal strength range. In this range strain localization is not so efficient that rifts can not overlap, but not so diffuse that they hardly interact at all.

The thickness of the brittle layer is speculated to determine the maximum X-offset for rift linkage (Allken et al., 2012; Vendeville & Le Calvez, 1995). In accordance with this, analogue experiments have had similar types of rift linkage at much smaller X-offsets than used in this study (Acocella, 2008; Tentler, 2003; Tentler & Acocella, 2010). However, recent lithosphere-

scale studies with thermal effects found that rifts can interact at offsets much larger than the brittle layer thickness (<400 km; Le Pourhiet et al., 2017). Our study finds that the 400 km limit is related to boundary conditions (supplementary Fig. S2), and that in larger domains rifts can still interact and form microplates with a 400 km X-offset. While we investigated the effects of lithosphere thickness on rift linkage, our models are too small to fully explore whether the brittle layer thickness affects the maximum X-offset for rift interaction in lithosphere-scale studies. Additionally, while we vary the lithosphere thickness we do not change our total crustal thickness. Different combinations of crustal setup and lithosphere thicknesses may result in different X-offset ranges for the regimes mentioned in this study.

In this study, transform faults are <200 km, which agrees with earlier studies (Allken et al., 2012; Taras Gerya, 2010, 2012, 2013a, 2013b; Püthe & Gerya, 2014), but in nature transform faults can range from <100 km to >1000 km (Boettcher & Jordan, 2004). Ammann et al. (2017) found that for transform faults >200 km to form, oblique extension is vital. Additionally, in large domains with low extensional velocity they find that overlap and microplate formation are favored over transform faults. This agrees with analogue models, which suggest that a larger total length of rift segments helps rift overlap (Acocella, 2008), while higher extensional obliquity promotes rift linkage (Acocella 2008, Zwaan et al., 2016). Thus, in large domains where microplate formation is more likely, a temporal change in extensional direction to a more oblique orientation, such as during the rifting of the South Atlantic (Heine et al., 2013), may help facilitate a rift jump and lead to a transform fault linking the rift segments attaching the microplate to one side.

While transform faults are an important factor in seafloor spreading, whether they form only during seafloor spreading (Eagles et al., 2015; Nguyen et al., 2016), or can initiate earlier in late-stage continental rifting, is still unclear. Illsley-Kemp et al. (2018) suggest that early proto-transform fault segments can rotate, forming pure strike-slip motion prior to seafloor spreading in magmatically active rift systems. Our results agree with their findings, as prior to seafloor spreading we observe the formation of short nearly pure strike-slip motion transform faults within the highly oblique proto-transform segment connecting some offset rifts (e.g., Fig. 3). Additionally, our results suggest that the inclusion of magmatic processes is not required to form such transform faults, and that transform faults can initiate within amagmatic continental rift systems.

4 Comparison of numerical models to two natural microplate settings

In this section we discuss how our models compare to two regions where evidence suggests there is a continental microplate, namely the Flemish Cap (Welford et al., 2012) and the Sao Paulo Plateau (Scotchman et al., 2010). We first compare the reference microplate model evolution to the Flemish Cap, formed during the rifting of the North Atlantic. Second, we focus on the formation of the Sao Paulo Plateau in the Santos Basin, which formed during the rifting of the South Atlantic.

4.1 The Flemish Cap geologic setting

The Flemish Cap is a 20-30 km thick continental block (continental ribbon) tethered to the rifted continental margin of offshore Newfoundland, eastern Canada (Funck, 2003; Gerlings et al., 2011; Keen & de Voogd, 1988) (Fig. 8b). The broader continental shelf offshore Newfoundland comprises the Grand Banks, the Bonavista Platform, and the Flemish Cap. It consists of basement rocks of the Avalon terrane, a Gondwanan terrane that was accreted to Laurentia

(North America) during the Palaeozoic closing of the Iapetus Ocean as part of the Appalachian Orogeny (Haworth & Keen, 1979; Williams, 1984, 1995). During the Mesozoic breakup of the supercontinent Pangaea, rifting and opening of the modern North Atlantic Ocean occurred within the Avalon terrane.

The Flemish Cap lies to the southeast of the deepwater Orphan Basin, out of which it is proposed to have originated (Le Pichon et al., 1977; Sibuet et al., 2004; Srivastava & Verhoef, 1992), with Sibuet et al. (2007) arguing for 43° of clockwise rotation from the Late Triassic to the Early Cretaceous and a further translation of 200-300 km southeastward, relative to North America, from the Late Jurassic to the early Aptian. The Orphan Basin is itself underlain by extended continental crust, with zones of hyperextension resolved using seismic refraction, reflection, and potential field methods (Chian et al., 2001; Gouiza et al., 2017; Lau et al., 2015; Watremez et al., 2015; Welford et al., 2012, 2020). One particularly striking feature of the Orphan Basin is the alignment of zones of hyperextended continental crust (highlighted by peach dashed lines in Fig. 8b) that have been interpreted as failed rifts (Chian et al., 2001; Welford et al., 2012, 2020). While the independent rotation of the Flemish Cap relative to North America has been successfully modelled by recent plate reconstructions, both rigid (Nirrengarten et al., 2018) and deformable (Peace et al., 2019), the precise mechanisms that led to the rotation of the Flemish Cap and the failure of rifts within the Orphan Basin are yet to be elucidated.

4.2 Flemish Cap comparison and discussion

We compare the first-order crustal architecture of the Flemish Cap to a mirrored version of the reference microplate model (300 km X-offset, 300 km Y-offset, 25:10 crustal ratio, 120 km lithosphere) at 30 Myr model time (Fig. 8c). This allows us to examine how rifting would evolve if initial rift placement had a different polarity of rift arm offset. In the model, a 240 km wide microplate core was rotated ~50° and 280 km off the western margin (measured in the X-direction along the center). A small region of oceanic crust formed from the obsolete western rift, and on the eastern side oceanic crust formed along most of the rift. The model had an eastern rift jump that attached the clockwise-rotating microplate to the western margin.

From the comparison of present-day crustal thicknesses across the Newfoundland margin (Fig. 8b) and the mirrored microplate modelling results (Fig. 8c), the microplate model successfully replicates the scale of the Flemish Cap rotating block, the approximate areal extent of rifting in the Orphan Basin, and the eastward rift jump outboard of Flemish Cap leading to the failure of the rifts in the Orphan Basin. The only major discrepancy could be argued to involve the extent of predicted oceanic crust generated in the failed rift branch. To date, no oceanic crust has been interpreted to underlie the Orphan Basin, although crustal velocities within the failed rift along profile W20 in Fig. 8d (Welford et al., 2020) do not definitively preclude the presence of oceanic crust.

The modelling results (Fig. 8c) reveal that the evolution from initial rift branch interaction, through microplate formation and rotation (~50°), to eventual rift branch failure, can be achieved in less than 35 Myr. This time window is significantly narrower than the Late Triassic to Early Cretaceous time scale proposed by Sibuet et al. (2007) for the Flemish Cap, which is due to the fact that the modelled constant extension velocity of 20 mm/yr (full rate) exceeds divergence velocities of the initial, slow rift phase in this region (Barnett-Moore et al., 2018; Brune et al., 2016; Peace et al., 2019). Nevertheless, careful seismic interpretation of reflection data within the Orphan Basin is still needed to better constrain the exact timing of the Flemish Cap rotation.

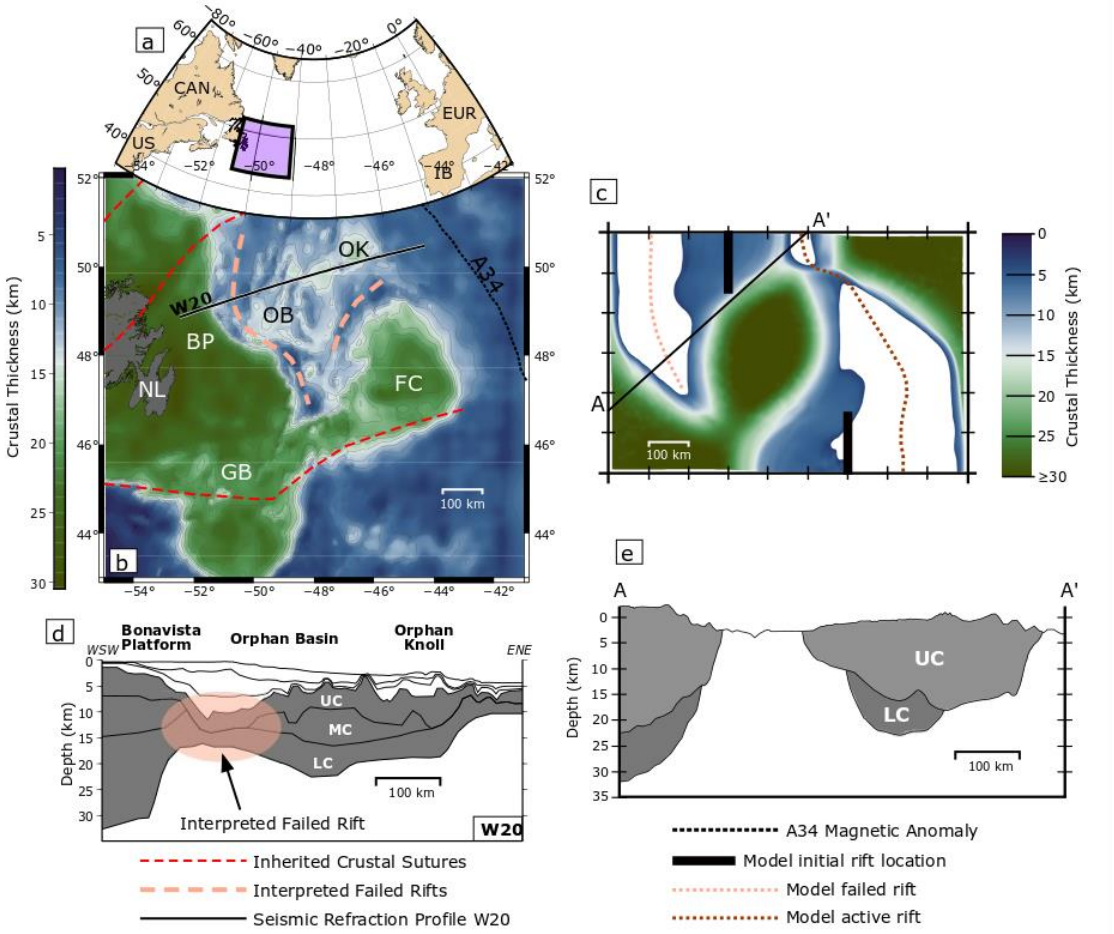

Figure 8: (a) Map of the North Atlantic with the extent of map (b) shown in purple; (b) crustal thickness of the offshore Newfoundland margin derived from constrained 3-D gravity inversion (using methodology of Welford et al., 2012); (c) simulated rift connections for a mirrored microplate model with clockwise rotation; (d) simplified crustal model from Welford et al. (2020) highlighting the interpreted failed rift in the western Orphan Basin. Magnetic anomaly A34 obtained from Srivastava et al. (1990); (e) Cross-section A-A' through the modelled microplate. Abbreviations: BP, Bonavista Platform; FC, Flemish Cap; GB, Grand Banks; NL, Newfoundland; OB, Orphan Basin; OK, Orphan Knoll; UC, Upper Crust; MC, Middle Crust; LC, Lower Crust.

Constrained 3D gravity inversions performed on the conjugate Flemish Cap/Orphan Basin and Irish Atlantic continental margins (Welford et al., 2012) have resolved significantly different rifting styles and compartmentalization. Specifically, on the Irish margin, hyperextended crust beneath sedimentary basins like the Porcupine Basin is abruptly juxtaposed against unstretched crustal blocks like the Porcupine Bank. By contrast, the crust beneath the Orphan Basin appears to have been stretched more uniformly. Based on geodynamic modelling results from Huismans & Beaumont (2011), Welford et al. (2012) argue that fundamental rheological differences controlled the different rifting styles across the conjugate pair and that a weak crustal layer underlies the Orphan Basin. This conclusion is consistent with the results displayed in Figure 7 where microplate formation and rotation is predicted for the models involving weaker crust.

4.3 Sao Paulo Plateau geologic setting

The Sao Paulo Plateau (SPP) is a marginal plateau (Kumar & Gambôa, 1979; Mohriak et al., 2010) occupying large parts of the Santos Basin on the Brazilian Atlantic margin. It is delimited landward by the wide continental shelf of the Santos Basin, by the Cabo Frio Transfer zone/Rio

de Janeiro Fracture Zone to the north, the oceanic crust in the east (approximately coinciding with the Jean Charcot seamounts) and the Sao Paulo escarpment/Florianopolis Fracture zone to the south. Water depths on the SPP range between 2000 m and more than 3000 m (Fig. 9b).

The Santos Basin and the SPP were formed during the early Cretaceous as part of the South Atlantic rift system (Chang et al.,1992; Heine et al., 2013; Meisling et al., 2001) and are situated just south of a major rift segment boundary between the central (conjugate Kwanza-Campos Basins) and the southern South Atlantic rift segment (conjugate Santos/Namibe Basins; Guiraud et al., 2010; Meisling et al., 2001). Here, the rift axis is offset to the east by about 300 km along the Cabo Frio-Benguela transform system. Continental extension between Africa and South America commenced in the early Cretaceous, rifting lithosphere composed of reworked Archean inliers, Neoproterozoic magmatic arcs and orogenic belts of the Brasiliano orogenic cycle, with a tectono-thermal age of the lithosphere of approximately Cambrian age (around 550-500 Ma; Neves et al., 2014). Approximately 10 Myrs into rifting, the Tristan da Cunha (TC) plume impinged on the South American plate, creating the Parana-Etendenka Large Igneous Province (Krob et al., 2020 and references therein; Heine et al., 2013), with the conjugate Walvis/Florianopolis ridges being one eruption center in the southern part of the Santos Basin. This magmatic episode with extensive extrusive basalt forms the present-day economic basement (Chang et al., 1992; Moreira et al., 2007). At the time of emplacement, the rift had been extended by approximately 100 km (Heine et al., 2013). Continued extension and waning magmatic budget resulted in a complex rift architecture obscured by a thick layer of Aptian-aged evaporites covering large parts of the basin. Several giant hydrocarbon discoveries in the pre-salt sequences are hosted in shallow water carbonate facies. Subsequent infill of the basin largely consists of mixed carbonate and clastic sediments, affected by complex salt tectonics (Moreira et al., 2007).

The nature of the crust underlying the SPP is debated. Nearly all hydrocarbon wells terminating in the pre-salt sequences throughout the Santos Basin have terminated in basaltic extrusives. Regional analyses using seismic reflection, refraction and potential field methods (e.g., Borges & Gambôa, 2015; Evain et al., 2015; Klingelhoefer et al., 2014; Meisling et al., 2001; Scotchman et al., 2010; Zalán et al., 2011) conclude that large parts of the Santos Basin and Sao Paulo Plateau are underlain by thin crust of 13-25 km of mixed continental to magmatic crustal type (”heterogenous crust”), thermal buoyancy induced by the Tristan plume has likely resulted in dynamic uplift causing shallow water conditions on the SPP, despite relatively thin crustal thicknesses observed across the plateau (e.g. Evain et al., 2015).

Despite the disagreements on crustal type underlying the SPP and the Santos Basin, the area shows characteristics of microplate formation (Heine et al., 2013; Moulin et al., 2013). In the SW part of the Santos Basin, an aborted oceanic spreading ridge propagator, the Abimael Ridge (sometimes referred to as Avedis ridge), has been identified (e.g., Chang et al., 1992; Meisling et al., 2001; Scotchman et al., 2010). Along the proximal margin of the Santos Basin, potential field data indicate a zone of en echelon Moho uplifts (Meisling et al., 2001) and crustal thinning, along with extensive seaward-dipping reflector sequences (SDRs) indicating accommodation space formation related to crustal extension during a magma-rich rift phase. A faulted base salt surface in the inner, western part of the Santos Basin and isolated graben structures such as the Merluza Graben area in the northern part of the basin (Magee et al., 2021), indicate that the Avedis ridge has been active at least until deposition of the extensive early Aptian-aged evaporite layer in the central South Atlantic. Towards the NE basin margin, this zone merges with the Cabo Frio-Benguela transform (Guiraud et al., 2010; Mohriak et al., 1995), which

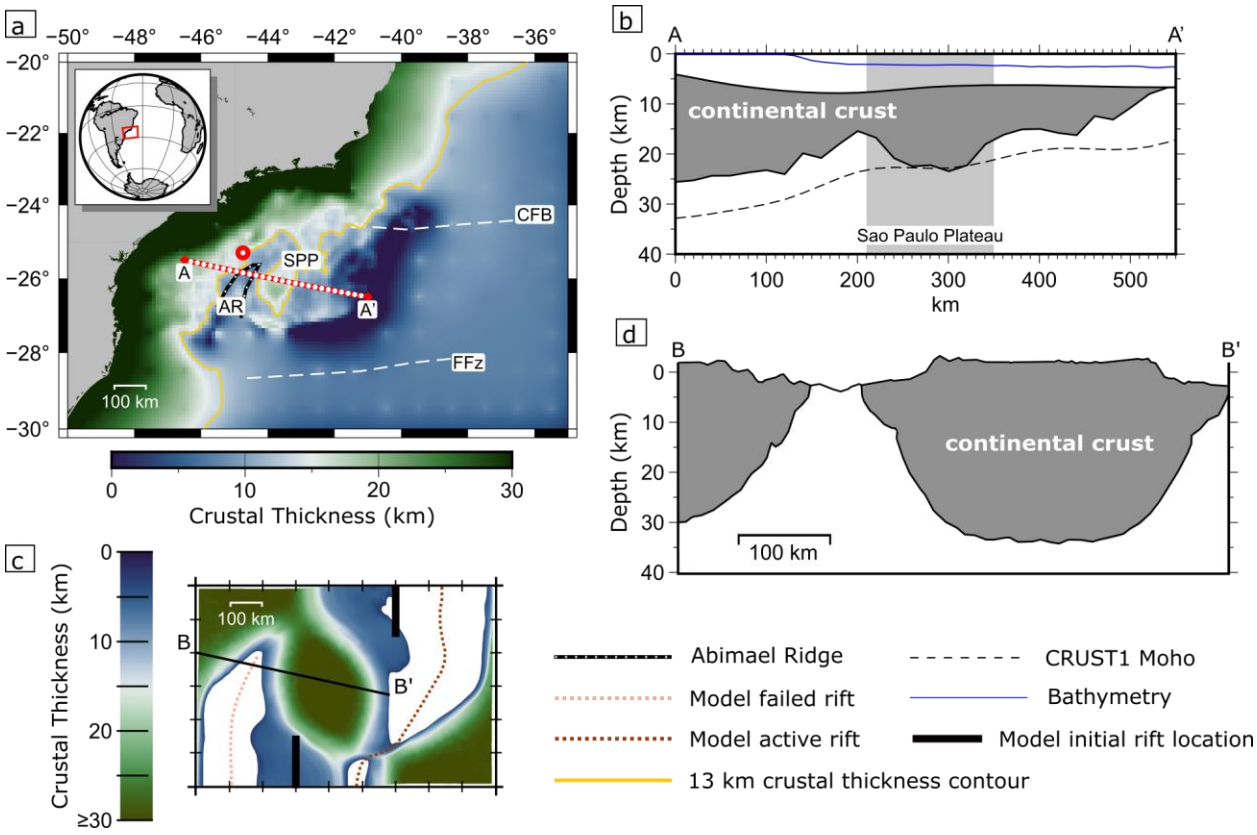

Figure 9: a) Map view of the Santos Basin region colored by continental crustal thickness (Shell proprietary data merged with resampled CRUST1 at 10 km resolution) showing the locations of the Sao Paulo Plateau (SPP) and the aborted Abimael ridge spreading propagator (AR), red dot indicates approximate position of Merluza Graben. Profile location indicated by red line, with markers spaced in 20 km intervals. Yellow contours show a crustal thickness of 13 km. CFB: Cabo Frio-Benguela Fracture zone, FFz: Florianopolis fracture zone. b) Cross-section along the A-A' profile: Top basement is extracted from resampled CRUST1 data (Bottom of lower sediments layer), lower solid black line is base of crust, computed by adding our crustal thickness estimate to resampled CRUST1 base of lower sediments. Water depth shown as thin in blue line (SRTM15+V2.1 at 10 km resolution). Gray box highlights the extent of the SPP microplate along the profile. (c) simulated rift connections for the reference microplate model (Fig. 4). (d) Cross-section B-B' through the modelled microplate.

laterally offsets the rift axis by about 500 km eastwards into the northerly adjoining Campos-Kwanza/Benguela rift segment. Crustal thickness observations and inverse models show that the eastern, distal part of the Santos Basin, east of the Sao Paulo Ridge/High is characterized by a second necking zone (Norton et al., 2016), which further thins the crust and eventually continues into steady-state oceanic crust (Mohriak et al., 2010).

Presently, plate kinematic reconstructions model an initial northward propagation of the southern South Atlantic oceanic spreading ridge into the Abimael Ridge region (Heine et al., 2013; Meisling et al., 2001; Moulin et al., 2013), of the western Santos Basin in pre-salt deposition times (i.e. pre late Albian), being laterally accommodated and offset by the Cabo Frio transform. The deformation focus/spreading ridge of the central South Atlantic is attempting to propagate southward, offset along the Angolan Benguela margin (Guiraud et al., 2010) and eventually overlapping with the Abimael Ridge for a limited amount of time until the Abimael Ridge becomes extinct and deformation is localised along the eastern margin of the Sao Paulo Plateau, forming a continuous spreading ridge connecting the central and south Atlantic rift segments (Heine et al., 2013; Moulin et al., 2013).

4.4 Sao Paulo Plateau comparison and discussion

In this section we compare the Sao Paulo Plateau to the reference microplate model at 30 Myr (300 km X-offset, 300 km Y-offset, 25:10 crustal ratio, 120 km lithosphere). The SPP represents a region of thickened crust that formed in a complex system influenced by the impingement of the TC plume, leading to the emplacement of large amounts of magmatic crust. Despite the plume's influence, the overall geometry of the plateau and western failed rift is comparable to the microplate modelled in this study. In both cases, a region of relatively thick crust (SPP) is encompassed by thinned crust from a failed western rift (Abimael Ridge region) to the west, and a dominant ocean-forming rift to the east.

Discrepancies between our models and the SPP arise in the size of the microplate and features in the surrounding region. The SPP crustal thickness ranges between 13-25 km and the core is ~140 km wide. This is both smaller and thinner than the microplate modelled in this study. The region is bounded by the Florianapolis fracture zone to the south. Analogue modelling suggests that hard rift linkage is facilitated with oblique rifting (Zwaan et al., 2016), thus it is possible that the region's directional change in extension may have favored the formation of transform faults to connect the overlapping rift segments.

One limitation in our model is that we do not include melt processes, which may be especially important in the SPP region with the arrival of the TC plume (Beniest et al., 2017; Lavecchia et al., 2017). Even though we do not include melting, we partially address this through an additional supplementary model (supplementary videos S5 and S6) where we include the arrival of a thermal mantle plume in two stages to represent the plume head and stem (similar to Bredow et al., 2017; Gassmöller et al., 2016; Koptev et al., 2015; Steinberger et al., 2019). Because the TC plume did not impinge on the region until ~10 Myr after rifting began, we prescribe the plume arrival in the model at 10 Myr and find that at this stage and without melt processes the plume does not drastically affect model evolution, but plume placement can influence the rift jump direction.

5 Conclusions

In this study we show that rift branches that are offset along (Y) or perpendicular (X) to strike connect in 4 ways: *Regime 1*) through an oblique rift, *Regime 2*) through a transform fault, *Regime 3*) by microplate formation with a rift jump to the dominant rift, or *Regime 4*) through a rift jump to the dominant rift without rift interaction. We find that the X-offset is the primary factor determining the connection type. The secondary factor is the effectiveness of plastic strain localization, which in this case relates to the crustal strength or lithosphere thickness. In weaker crust, the integrated brittle strength is lower and the models are less susceptible to plastic weakening, which leads to more diffuse rift propagation. This diffuse propagation promotes rift overlap, which slows rift propagation, causing rotation and microplate formation. In stronger crust with higher integrated brittle strength, plastic strain is more localized and rift connection becomes more efficient; in these cases microplates do not form and oblique and transform fault connections occur at larger X-offsets.

The microplates modelled in this study exhibit a core of poorly thinned continental crust that has been rotated (counter-clockwise for right-stepping rift segments, clockwise for left-stepping ones). Pronounced thinning occurred on both sides of the microplate from two coexisting rifts, with an oceanward rift jump rendering the landward rift obsolete. Early rift geometries and

interactions in the microplate models resemble the East African Rift System and show that overlapping rifts with a rotating microplate can form without the guidance of lithospheric strength heterogeneities (e.g., mobile belts; Glerum et al. 2020). Additionally, the reference model elucidates many features of the Flemish Cap and Sao Paulo Plateau, two extensional microplates that formed during the rifting of the North and South Atlantic, respectively. In both regions there exists thinning to both sides of a relatively thick core that has been rotated oceanward off the margin. Both areas are also associated with a landward failed rift and a likely rift jump to the dominant ocean-forming rift. Beyond these two examples, our modelled evolution of microplate kinematics could be a template to understand the formation of other continental promontories at rifted margins across a range of scales worldwide, such as the Galicia, Porcupine, and Rockall Banks, the Faroes/Fugloy ridge, Jan Mayen, the NE Brazil Borborema Province/Sergpipe Block, the Falkland Islands microcontinent, the Exmouth Plateau on the Australian NW Shelf, and Sri Lanka.

Acknowledgments, Samples, and Data

This study was conducted within the Helmholtz Young Investigators Group CRYSTALS (VH-NG-1132). We thank the Computational Infrastructure for Geodynamics (geodynamics.org), which is funded by the National Science Foundation under award EAR- 0949446 and EAR-1550901, for supporting the development of ASPECT. Computations were performed on the German computer clusters Konrad and Emmy, both HLRN facilities. Figures in this paper were made with ParaView, the Generic Mapping Tools (Wessel et al., 2019), and InkScape, and color scales are from Crameri (2018). We thank Shell Global Solutions International B.V. for the permission to publish the higher resolution crustal thickness data for the Santos Basin which was kindly provided by Lorcan Kennan. All models were run using deal.II 9.1.1, and the ASPECT version with all model parameter files found here: https://doi.org/10.5281/zenodo.4601188. We would like to thank the reviewers Laetitia Le Pourhiet, Alexander Koptev, and Michael Nirrengarten for their detailed and constructive feedback on this manuscript.

References

Acocella, V. (2008). Transform faults or Overlapping Spreading Centers? Oceanic ridge interactions revealed by analogue models. *Earth and Planetary Science Letters*, *265*(3–4), 379–385. https://doi.org/10.1016/j.epsl.2007.10.025

Allken, V., Huismans, R. S., & Thieulot, C. (2011). Three-dimensional numerical modeling of upper crustal extensional systems. *Journal of Geophysical Research: Solid Earth*, *116*(10), 1–15. https://doi.org/10.1029/2011JB008319

Allken, V., Huismans, R. S., & Thieulot, C. (2012). Factors controlling the mode of rift interaction in brittle-ductile coupled systems: A 3D numerical study. *Geochemistry, Geophysics, Geosystems*, *13*(5), 1–18. https://doi.org/10.1029/2012GC004077

Ammann, N., Liao, J., Gerya, T., & Ball, P. (2017). Oblique continental rifting and long transform fault formation based on 3D thermomechanical numerical modeling. *Tectonophysics*, (February), 1–16. https://doi.org/10.1016/j.tecto.2017.08.015

Araujo Borges, T., & Gambôa, L. A. P. (2015). Sismoestratigrafia Do Limite Sul Da Bacia de Santos e Suas Implicações Na Evolução Do Atlântico Sul Primordial. *Boletim de Geociências Da Petrobras*, *23*(1/2). Retrieved from

http://publicacoes.petrobras.com.br/main.jsp?lumPageId=8A9E308F545405DE0154A04B46AD0C9E&lumItemId=8A9D2AAF5CA274FD015D746F91B218E5&previewItemId=8A9D2AAF5CA274FD015D746F91A818E4&publicacaoId=8A9D2AAF5A284744015A2958DE4D3BC9&lastItem=1

Artemieva, I. M. (2006). Global 1° × 1° thermal model TC1 for the continental lithosphere: Implications for lithosphere secular evolution. *Tectonophysics*, *416*(1–2), 245–277. https://doi.org/10.1016/j.tecto.2005.11.022

Artemieva, I. M., & Mooney, W. D. (2001). Thermal thickness and evolution of Precambrian lithosphere: A global study. *Journal of Geophysical Research: Solid Earth*, *106*(B8), 16387–16414. https://doi.org/https://doi.org/10.1029/2000JB900439

Bahadori, A., & Holt, W. E. (2019). Geodynamic evolution of southwestern North America since the Late Eocene. *Nature Communications*, *10*(1), 5213. https://doi.org/10.1038/s41467-019-12950-8

Bangerth, W., Dannberg, J., Gassmoeller, R., & Heister, T. (2019). ASPECT v2.1.0. *Zenodo*. Retrieved from https://doi.org/10.5281/zenodo.2653531

Barnett-Moore, N., Müller, D. R., Williams, S., Skogseid, J., & Seton, M. (2018). A reconstruction of the North Atlantic since the earliest Jurassic. *Basin Research*, *30*, 160–185. https://doi.org/10.1111/bre.12214

Beniest, A., Koptev, A., Leroy, S., Sassi, W., & Guichet, X. (2017). Two-Branch Break-up Systems by a Single Mantle Plume: Insights from Numerical Modeling. *Geophysical Research Letters*, *44*(19), 9589–9597. https://doi.org/https://doi.org/10.1002/2017GL074866

Boettcher, M. S., & Jordan, T. H. (2004). Earthquake scaling relations for mid-ocean ridge transform faults. *Journal of Geophysical Research : Solid Earth*, *109*(2), 1–21.

Bredow, E., Steinberger, B., Gassmöller, R., & Dannberg, J. (2017). How plume-ridge interaction shapes the crustal thickness pattern of the Réunion hotspot track. *Geochemistry, Geophysics, Geosystems*, *18*(8), 2930–2948. https://doi.org/10.1002/2017GC006875

Brune, S., Corti, G., & Ranalli, G. (2017). Controls of inherited lithospheric heterogeneity on rift linkage: Numerical and analog models of interaction between the Kenyan and Ethiopian rifts across the Turkana depression. *Tectonics*, *36*(9), 1767–1786. https://doi.org/10.1002/2017TC004739

Brune, S., Heine, C., Clift, P. D., & Pérez-Gussinyé, M. (2017). Rifted margin architecture and crustal rheology: Reviewing Iberia-Newfoundland, Central South Atlantic, and South China Sea. *Marine and Petroleum Geology*, *79*, 257–281. https://doi.org/10.1016/j.marpetgeo.2016.10.018

Brune, S., Heine, C., Pérez-Gussinyé, M., & Sobolev, S. V. (2014). Rift migration explains continental margin asymmetry and crustal hyper-extension. *Nature Communications*, *5*, 1–9. https://doi.org/10.1038/ncomms5014

Brune, S., Williams, S. E., Butterworth, N. P., & Müller, R. D. (2016). Abrupt plate accelerations shape rifted continental margins. *Nature*, *536*(7615), 201–204.

https://doi.org/10.1038/nature18319

Buiter, S. J. H., & Torsvik, T. H. (2014, September 1). A review of Wilson Cycle plate margins: A role for mantle plumes in continental break-up along sutures? *Gondwana Research*. Elsevier Inc. https://doi.org/10.1016/j.gr.2014.02.007

Calais, E., Ebinger, C., Hartnady, C., & Nocquet, J. M. (2006). Kinematics of the East African Rift from GPS and earthquake slip vector data. *Geological Society, London, Special Publications*, *259*, 9–22.

Chang, H. K., Kowsmann, R. O., Figueiredo, A. M. F., & Bender, A. (1992). Tectonics and Stratigraphy of the East Brazil Rift System: An Overview. *Tectonophysics*, *213*(1–2), 97–138. https://doi.org/10.1016/0040-1951(92)90253-3

Chian, D., Reid, I., & Jackson, H. (2001). Crustal structure beneath Orphan Basin and implications for nonvolcanic continental rifting. *Journal of Geophysical Research*, *106*, 10,923-10,940.

Corti, G., Cioni, R., Franceschini, Z., Sani, F., Scaillet, S., Molin, P., … Glerum, A. (2019). Aborted propagation of the Ethiopian rift caused by linkage with the Kenyan rift. *Nature Communications*, *10*(1), 1–11. https://doi.org/10.1038/s41467-019-09335-2

Crameri, F. (2018). Scientific colour maps. Zenodo. https://doi.org/http://doi.org/10.5281/zenodo.1243862

Davis, R. O., & Selvadurai, A. P. . (2002). *Plasticity and Geomechanics*. Cambridge University Press.

de Wit, M. J., Stankiewicz, J., & Reeves, C. (2008). Restoring pan-African-Brasiliano connections: More Gondwana control, less Trans-Atlantic corruption. *Geological Society Special Publication*, *294*, 399–412. https://doi.org/10.1144/SP294.20

Dubinin, E. P., Grokholsky, A. L., & Makushkina, A. I. (2018). Physical modeling of the formation conditions of microcontinents and continental marginal plateaus. *Izvestiya, Physics of the Solid Earth*, *54*(1), 66–78. https://doi.org/10.1134/S1069351318010056

Eagles, G., Pérez-Díaz, L., & Scarselli, N. (2015). Getting over continent ocean boundaries. *Earth-Science Reviews*, *151*, 244–265.

Eagles, G., Gloaguen, R., & Ebinger, C. (2002). Kinematics of the Danakil microplate. *Earth and Planetary Science Letters*, *203*(2), 607–620. https://doi.org/10.1016/S0012-821X(02)00916-0

Evain, M., Afilhado, A., Rigoti, C., Loureiro, A., Alves, D., Klingelhoefer, F., … Aslanian, D. (2015). Deep Structure of the Santos Basin-São Paulo Plateau System, SE Brazil. *Journal of Geophysical Research: Solid Earth*, *120*, 5401–5431. https://doi.org/10.1002/2014jb011561

Funck, T. (2003). Crustal structure of the ocean-continent transition at Flemish Cap: Seismic refraction results. *Journal of Geophysical Research*, *108*(B11), 1–20. https://doi.org/10.1029/2003jb002434

Gassmoller, R., Dannberg, J., Bredow, E., Steinberger, B., & Torsvik, T. H. (2016). Major influence of plume-ridge interaction, lithosphere thickness variations, and global mantle

flow on hotspot volcanism—The example of Tristan. *Geochemistry Geophysics Geosystems*, 1454–1479. https://doi.org/doi:10.1002/ 2015GC006177

Gerlings, J., Louden, K. E., & Jackson, H. R. (2011). Crustal structure of the Flemish Cap Continental Margin (eastern Canada): An analysis of a seismic refraction profile. *Geophysical Journal International*, *185*(1), 30–48. https://doi.org/10.1111/j.1365-246X.2011.04931.x

Gernigon, L., Gaina, C., Olesen, O., Ball, P. J., Péron-Pinvidic, G., & Yamasaki, T. (2012). The Norway Basin revisited: From continental breakup to spreading ridge extinction. *Marine and Petroleum Geology*, *35*(1), 1–19. https://doi.org/10.1016/j.marpetgeo.2012.02.015

Gerya, Taras. (2010). Dynamical Instability Produces Transform Faults at Mid-Ocean Ridges. *Science*, *329*(August), 1047–1050. https://doi.org/10.1126/science.1189134

Gerya, Taras. (2012). Origin and models of oceanic transform faults. *Tectonophysics*, *522–523*, 34–54. https://doi.org/10.1016/j.tecto.2011.07.006

Gerya, Taras. (2013a). Initiation of transform faults at rifted continental margins: 3D petrological-thermomechanical modeling and comparison to the Woodlark Basin. *Petrology*, *21*(6), 550–560.

Gerya, Taras. (2013b). Three-dimensional thermomechanical modeling of oceanic spreading initiation and evolution. *Physics of the Earth and Planetary Interiors*, *214*, 35–52. https://doi.org/10.1016/j.pepi.2012.10.007

Gerya, T V, Stern, R. J., Baes, M., Sobolev, S. V, & Whattam, S. A. (2015). Plate tectonics on the Earth triggered by plume-induced subduction initiation. *Nature*, *527*(7577), 221–225. https://doi.org/10.1038/nature15752

Gibbons, A. D., Whittaker, J. M., & Müller, R. D. (2013). The breakup of East Gondwana: Assimilating constraints from Cretaceous ocean basins around India into a best-fit tectonic model. *Journal of Geophysical Research: Solid Earth*, *118*(3), 808–822. https://doi.org/https://doi.org/10.1002/jgrb.50079

Glerum, A., Brune, S., Stamps, D. S., & Strecker, M. R. (2020). Victoria continental microplate dynamics controlled by the lithospheric strength distribution of the East African Rift. *Nature Communications*, *11*(1), 1–15. https://doi.org/10.1038/s41467-020-16176-x

Glerum, A., Thieulot, C., Fraters, M., Blom, C., & Spakman, W. (2018). Nonlinear viscoplasticity in ASPECT: Benchmarking and applications to subduction. *Solid Earth*, *9*(2), 267–294. https://doi.org/10.5194/se-9-267-2018

Gouiza, M., Hall, J., & Welford, J. K. (2017). Tectono-stratigraphic evolution and crustal architecture of the Orphan Basin during North Atlantic rifting. *International Journal of Earth Sciences*, *106*(3), 917–937. https://doi.org/10.1007/s00531-016-1341-0

Guiraud, M., Buta-Neto, A., & Quesne, D. (2010). Segmentation and Differential Post-Rift Uplift at the Angola Margin as Recorded by the Transform-Rifted Benguela and Oblique-to-Orthogonal-Rifted Kwanza Basins. *Marine and Petroleum Geology*, *27*(5), 1040–1068. https://doi.org/10.1016/j.marpetgeo.2010.01.017

Haworth, R., & Keen, C. E. (1979). The Canadian Atlantic margin: a passive continental margin

encompassing an active past. *Tectonophysics*, *59*, 83–126.

Heckenbach, E. L., Brune, S., Glerum, A. C., & Bott, J. (2021). Is there a Speed Limit for the Thermal Steady-State Assumption in Continental Rifts? *Geochemistry, Geophysics, Geosystems*, *n/a*(n/a), e2020GC009577. https://doi.org/https://doi.org/10.1029/2020GC009577

Heidbach, O., Reinecker, J., Tingay, M., Müller, B., Sperner, B., Fuchs, K., & Wenzel, F. (2007). Plate boundary forces are not enough: Second- and third-order stress patterns highlighted in the World Stress Map database. *Tectonics*, *26*(6), 1–19. https://doi.org/10.1029/2007TC002133

Heine, C, & Müller, R. D. (2005). Late Jurassic rifting along the Australian North West Shelf: margin geometry and spreading ridge configuration. *Australian Journal of Earth Sciences*, *52*(1), 27–39. https://doi.org/10.1080/08120090500100077

Heine, Christian, Zoethout, J., & Müller, R. D. (2013). Kinematics of the South Atlantic rift. *Solid Earth*, *4*(2), 215–253. https://doi.org/10.5194/se-4-215-2013

Heister, T., Dannberg, J., Gassmöller, R., & Bangerth, W. (2017). High Accuracy Mantle Convection Simulation through Modern Numerical Methods – II: Realistic Models and Problems. *Geophysical Journal International*, *210*, 833–851. https://doi.org/doi:10.1093/gji/ggx195

Heron, P. J., Peace, A. L., McCaffrey, K. J. W., Welford, J. K., Wilson, R., van Hunen, J., & Pysklywec, R. N. (2019). Segmentation of Rifts Through Structural Inheritance: Creation of the Davis Strait. *Tectonics*, *38*(7), 2411–2430. https://doi.org/10.1029/2019TC005578

Hirth, G., & Kohlstedt, D. (2003). Rheology of the upper mantle and the mantle wedge: a view from the experimentalists. *Inside the Subudction Factory Geophysical Monograph (American Geophysical Union)*, *183*.

Huismans, R., & Beaumont, C. (2011). Depth-dependent extension, two-stage breakup and cratonic underplating at rifted margins. *Nature*, *473*, 74–78.

Illsley-Kemp, F., Bull, J. M., Keir, D., Gerya, T., Pagli, C., Gernon, T., … Kendall, J. M. (2018). Initiation of a Proto-transform Fault Prior to Seafloor Spreading. *Geochemistry, Geophysics, Geosystems*, *19*(12), 4744–4756. https://doi.org/10.1029/2018GC007947

Jourdon, A., Le Pourhiet, L., Mouthereau, F., & May, D. (2020). Modes of Propagation of Continental Breakup and Associated Oblique Rift Structures. *Journal of Geophysical Research: Solid Earth*, *125*(9), 1–27. https://doi.org/10.1029/2020JB019906

Karato, S., & Wu, P. (1993). Rheology the Upper Mantle : Synthesis, *260*(May).

Katz, R. F., Ragnarsson, R., & Bodenschatz, E. (2005). Tectonic microplates in a wax model of sea-floor spreading. *New Journal of Physics*, *7*. https://doi.org/10.1088/1367-2630/7/1/037

Keary, P., Klepeis, K. A., & Vine, F. J. (2009). *Global Tectonics*. John Wiley & Sons, LTD.

Keen, C., & de Voogd, B. (1988). The continent-ocean boundary at the rifted margin of eastern Canada: new results from deep seismic reflection stud- ies. *Tectonics*, *7*, 107–124.

King, M. T., Welford, J. K., & Peace, A. L. (2020). Investigating the role of the Galicia Bank on

the formation of the North West Iberian margin using deformable plate tectonic models. *Tectonophysics*, *789*, 228537. https://doi.org/10.1016/j.tecto.2020.228537

Klingelhoefer, F., Evain, M., Afilhado, A., Rigoti, C., Loureiro, A., Alves, D., … Aslanian, D. (2014). Imaging Proto-Oceanic Crust off the Brazilian Continental Margin. *Geophysical Journal International*, *200*(1), 471–488. https://doi.org/10.1093/gji/ggu387

Koptev, A. I., & Ershov, A. V. (2011). Thermal thickness of the Earth's lithosphere: a numerical model. *Moscow University Geology Bulletin*, *66*(5), 323–330. https://doi.org/10.3103/S014587521105005X

Koptev, A, Calais, E., Burov, E., Leroy, S., & Gerya, T. (2015). Dual continental rift systems generated by plume–lithosphere interaction. *Nature Geoscience*, *8*(5), 388–392. https://doi.org/10.1038/ngeo2401

Koptev, Alexander, Burov, E., Gerya, T., Le Pourhiet, L., Leroy, S., Calais, E., & Jolivet, L. (2018). Plume-induced continental rifting and break-up in ultra-slow extension context: Insights from 3D numerical modeling. *Tectonophysics*, *746*, 121–137. https://doi.org/10.1016/j.tecto.2017.03.025

Krob, F. C., Glasmacher, U. A., Bunge, H.-P., Friedrich, A. M., & Hackspacher, P. C. (2020). Application of Stratigraphic Frameworks and Thermochronological Data on the Mesozoic SW Gondwana Intraplate Environment to Retrieve the {{Paraná}}-{{Etendeka}} Plume Movement. *Gondwana Research*, *84*, 81–110. https://doi.org/10.1016/j.gr.2020.02.010

Kronbichler, M., Heister, T., & Bangerth, W. (2012). High Accuracy Mantle Convection Simulation through Modern Numerical Methods. *Geophysical Journal International*, *191*. https://doi.org/doi:10.1111/j.1365-246x.2012.05609.x.

Kumar, N., & Gambôa, L. a. P. (1979). Evolution of the São Paulo Plateau (Southeastern Brazilian Margin) and Implications for the Early History of the South Atlantic. *GSA Bulletin*, *90*(3), 281–293. https://doi.org/10.1130/0016-7606(1979)90<281:EOTSPP>2.0.CO;2

Lau, K. H., Watremez, L., E., L. K. ., & Nedimovic, M. R. (2015). Structure of thinned continental crust across the Orphan Basin from a dense wide- angle seismic profile and gravity data. *Geophysical Journal International*, *202*, 1969–1992.

Lavecchia, A., Thieulot, C., Beekman, F., Cloetingh, S., & Clark, S. (2017). Lithosphere erosion and continental breakup: Interaction of extension, plume upwelling and melting. *Earth and Planetary Science Letters*, *467*, 89–98. https://doi.org/10.1016/j.epsl.2017.03.028

Le Calvez, J. H., & Vendeville, B. C. (2002). Experimental designs to model along- strike fault interaction. *Journal of the Virtual Explorer*, *7*(November). https://doi.org/10.3809/jvirtex.2002.00043

Le Pichon, X., Sibuet, J. C., & Francheteau, J. (1977). The fit of continent around the North Atlantic Ocean. *Tectonophysics*, *38*.

Le Pourhiet, L., Chamot-Rooke, N., Delescluse, M., May, D. A., Watremez, L., & Pubellier, M. (2018). Continental break-up of the South China Sea stalled by far-field compression. *Nature Geoscience*, *11*(8), 605–609. https://doi.org/10.1038/s41561-018-0178-5

Le Pourhiet, L., May, D. A., Huille, L., Watremez, L., & Leroy, S. (2017). A genetic link between transform and hyper-extended margins. *Earth and Planetary Science Letters*, *465*, 184–192. https://doi.org/10.1016/j.epsl.2017.02.043

Longley, I.M. Buessenschuett, C. Clydsdale, L., Cubitt, C. J., Davis, R. C., Johnson, M. K., Marshall, N. M., Murray, A. P., … Thompson, N. B. (2002). The North West Shelf of Australia - A Woodside Perspective. *In M. Keep and S. Moss, Editors, The Sedimentary Basins of Western Australia 3, Volume 3 of Proceedings of the Petroleum Exploration Society of Australia Symposium, Perth, Petroleum Exploration Society of Australia.*, *3*. Retrieved from http://www.searchanddiscovery.com/documents/longley/.

Macdonald, K. C., Scheirer, D. S., & Carbotte, S. M. (1991). Mid-ocean ridges: Discontinuities, segments and giant cracks. *Science*, *253*(5023), 986–994. https://doi.org/10.1126/science.253.5023.986

Magee, C., Pichel, L. M., Madden-Nadeau, A. L., Jackson, C. A.-L., & Mohriak, W. (2021). Salt–magma interactions influence intrusion distribution and salt tectonics in the Santos Basin, offshore Brazil. *Basin Research*, *n/a*(n/a). https://doi.org/https://doi.org/10.1111/bre.12537

Meisling, K. E., Cobbold, P. R., & Mount, V. S. (2001). Reactivation of an Obliquely Rifted Margin, Campos and Santos Basins, Southeastern Brazil. *AAPG Bulletin*, *85*, 1903–1924. https://doi.org/10.1306/8626D0B3-173B-11D7-8645000102C1865D

Mohriak, W. U., J. M. Macedo, R. T. Castellani, H. D. Rangel, A. Z. N. Barros, M. A. L., Latgé, J. A. Ricci, A. M. P. Mizusaki, P. Szatmari, L. S. Demercian, J. G. R., & Aires, J. R. (1995). Salt Tectonics and Structural Styles in the Deep-Water Province of the Cabo Frio Region, Rio de Janeiro, Brazil. *Salt Tectonics: A Global Perspective*, (July 2015), 273–304. https://doi.org/10.1306/m65604c13

Mohriak, W. U., Nóbrega, M., Odegard, M. E., Gomes, B. S., & Dickson, W. G. (2010). Geological and Geophysical Interpretation of the Rio Grande Rise, South-Eastern Brazilian Margin: Extensional Tectonics and Rifting of Continental and Oceanic Crusts. *Petroleum Geoscience*, *16*(3), 231–245. https://doi.org/10.1144/1354-079309-910

Mooney, W. D. (2010). *Crust and Lithospheric Structure - Global Crustal Structure*. *Treatise on Geophysics: Second Edition* (Vol. 1). Published by Elsevier Inc. https://doi.org/10.1016/B978-0-444-53802-4.00010-5

Moreira, J. L. P., Madeira, C. V., Gil, J. A., & Machado, M. A. P. (2007). Bacia de Santos. *Boletim de Geociências Da Petrobras*, *15*(2), 531–549. Retrieved from http://publicacoes.petrobras.com.br/main.jsp?lumPageId=8A9E308F545405DE0154A04B46AD0C9E&lumItemId=8A9D2A985A2833C5015B1A2064E029CF&previewItemId=8A9D2A985A2833C5015B1A2064D529CE&publicacaoId=8A9D2AAF5A284744015A2958DE4D3BC9#

Moulin, M., Aslanian, D., Rabineau, M., & Matias, L. (2013). Kinematic keys of the Santos-Namibe basins. *Geological Society, London, Special Publications*, *369*. https://doi.org/10.1144/SP369.3

Müller, R. D., Gaina, C., Roest, W. R., & Hansen, D. L. (2001). A recipe for microcontinent

formation. *Geology*, *29*(3), 203–206. https://doi.org/10.1130/0091-7613(2001)029<0203:arfmf>2.0.co;2

Muluneh, A. A., Brune, S., Illsley-Kemp, F., Corti, G., Keir, D., Glerum, A., … Mori, J. (2020). Mechanism for Deep Crustal Seismicity: Insight From Modeling of Deformation Processes at the Main Ethiopian Rift. *Geochemistry, Geophysics, Geosystems*, *21*(7), e2020GC008935. https://doi.org/https://doi.org/10.1029/2020GC008935

Naar, D. F., & Hey, R. N. (1991). Tectonic evolution of the Easter microplate. *Journal of Geophysical Research*, *96*(B5), 7961–7993. https://doi.org/10.1029/90JB02398

Naliboff, J. B., Glerum, A., Brune, S., Péron-Pinvidic, G., & Wrona, T. (2020). Development of 3-D Rift Heterogeneity Through Fault Network Evolution. *Geophysical Research Letters*, *47*(13), e2019GL086611. https://doi.org/https://doi.org/10.1029/2019GL086611

Naliboff, J., & Buiter, S. J. H. (2015). Rift reactivation and migration during multiphase extension. *Earth and Planetary Science Letters*, *421*, 58–67. https://doi.org/10.1016/j.epsl.2015.03.050

Neves, B. B. de B., Fuck, R. A., Pimentel, M. M., Neves, B. B. de B., Fuck, R. A., & Pimentel, M. M. (2014). The Brasiliano Collage in South America: A Review. *Brazilian Journal of Geology*, *44*(3), 493–518. https://doi.org/10.5327/Z2317-4889201400030010

Nguyen, L. C., Hall, S. A., Bird, D. E., & Ball, P. J. (2016). Reconstruction of the East Africa and Antarctica continental margins. *Journal OfGeophysical Research: Solid Earth*, *121*, 4156–4179.

Nirrengarten, M., Manatschal, G., Tugend, J., Kusznir, N., & Sauter, D. (2018). Kinematic evolution of the southern North Atlantic: implications for the formation of hyperextended rift systems. *Tectonics*, *37*, 89–118.

Norton, I. O., Carruthers, D. T., & Hudec, M. R. (2016). Rift to Drift Transition in the South Atlantic Salt Basins: A New Flavor of Oceanic Crust. *Geology*, *44*(1), 55–58. https://doi.org/10.1130/g37265.1

Pasyanos, M. E., Masters, T. . G., Laske, G., & Ma, Z. (2014). LITH1.0: An updated crust and lithospheric model of the Earth. *Journal of Geophysical Research: Solid Earth*, *119*, 2153–2173. https://doi.org/10.1002/2014JB011376.Received

Peace, A. L., Welford, J. K., Ball, P. J., & Nirrengarten, M. (2019). Deformable plate tectonic models of the southern North Atlantic. *Journal of Geodynamics*, *8*, 11–37.

Perez-Gussinye, M., Andres-Martinez, Miguel, Araujo, M., Xin, Y., Armitage, J. J., & Morgan, J. P. (2020). Lithospheric Strength and Rift Migration controls on Synrift Stratigraphy and Breakup Unconformities at Rifted Margins: Examples from Numerical Models, the Atlantic and South China Sea Margins. *Tectonics*. https://doi.org/https://doi.org/10.1029/2020TC006255

Péron-Pinvidic, G., & Manatschal, G. (2010). From microcontinents to extensional allochthons: Witnesses of how continents rift and break apart. *Petroleum Geoscience*, *16*(3), 189–197. https://doi.org/10.1144/1354-079309-903

Premarathne, U., Suzuki, N., Ratnayake, N., & Kularathne, C. (2016). BURIAL AND

613 THERMAL HISTORY MODELLING OF THE MANNAR BASIN, OFFSHORE SRI
614 LANKA. *Journal of Petroleum Geology*, *39*(2), 193–213.
615 https://doi.org/https://doi.org/10.1111/jpg.12640

616 Püthe, C., & Gerya, T. (2014). Dependence of mid-ocean ridge morphology on spreading rate in
617 numerical 3-D models. *Gondwana Research*, *25*(1), 270–283.
618 https://doi.org/10.1016/j.gr.2013.04.005

619 Rose, I., Buffett, B., & Heister, T. (2017). Stability and Accuracy of Free Surface Time
620 Integration in Viscous Flows. *Physics of the Earth and Planetary Interiors*, *262*, 90–100.
621 https://doi.org/doi:10.1016/j.pepi.2016.11.007

622 Rutter, E. H., & Brodie, K. H. (2004). Experimental grain size-sensitive flow of hot-pressed
623 Brazilian quartz aggregates. *Journal of Structural Geology*, *26*(11), 2011–2023.
624 https://doi.org/10.1016/j.jsg.2004.04.006

625 Rybacki, E., Gottschalk, M., Wirth, R., & Dresen, G. (2006). Influence of water fugacity and
626 activation volume on the flow properties of fine-grained anorthite aggregates. *Journal of*
627 *Geophysical Research: Solid Earth*, *111*(3). https://doi.org/10.1029/2005JB003663

628 Sandiford, D., Brune, S., Glerum, A., Naliboff, J., & Joanne, M. (n.d.). Kinematics of footwall
629 exhumation at oceanic detachment faults : solid-block rotation and apparent unbending.
630 *[Preprint]*, 1–25. https://doi.org/https://doi.org/10.1002/essoar.10506103.1

631 Schouten, H., Klitgord, K., Gallo, G. (1993). Edge-Driven Microplate Kinematics. *Journal of*
632 *Geophysical Research*, *98*, 6689–6701.

633 Scotchman, I. C., Gilchrist, G., Kusznir, N. J., Roberts, A. M., & Fletcher, R. (2010). The
634 Breakup of the South Atlantic Ocean: Formation of Failed Spreading Axes and Blocks of
635 Thinned Continental Crust in the Santos Basin, Brazil and Its Consequences for Petroleum
636 System Development. *Petroleum Geology Conference Series*, *7*, 855–866.
637 https://doi.org/10.1144/0070855

638 Sibuet, J. C., Srivastava, S. P., Enachescu, M., & Karner, G. D. (2007). Early Cretaceous motion
639 of Flemish Cap with respect to North America: Implications on the formation of Orphan
640 Basin and SE Flemish Cap-Galicia Bank conjugate margins. *Geological Society Special*
641 *Publication*, *282*, 63–76. https://doi.org/10.1144/SP282.4

642 Sibuet, Jean Claude, Srivastava, S. P., & Spakman, W. (2004). Pyrenean orogeny and plate
643 kinematics. *Journal of Geophysical Research: Solid Earth*, *109*(8), 1–18.
644 https://doi.org/10.1029/2003JB002514

645 Srivastava, S., Roest, W., Kovacs, L., Oakey, G., Le vesque, S., Verhoef, J., & Macnab, R.
646 (1990). Motion of Iberia since the Late Jurassic: results from detailed aeromagnetic
647 measurements in the Newfoundland Basin. *Tectonophysics*, *184*, 229–260.

648 Srivastava, S., & Verhoef, J. (1992). Evolution of Mesozoic sedimentary basins around the North
649 Central Atlantic: a preliminary plate kinematic solution. *Geological Society, London,*
650 *Special Publications*, *62*, 397–420.

651 Stamps, D. Sarah, Calais, E., Saria, E., Hartnady, C., Nocquet, J. M., Ebinger, C. J., &
652 Fernandes, R. M. (2008). A kinematic model for the East African Rift. *Geophysical*

Research Letters, *35*(5), 1–6. https://doi.org/10.1029/2007GL032781

Stamps, D S, Kreemer, C., Fernandes, R., Rajaonarison, T. A., & Rambolamanana, G. (2021). Redefining East African Rift System kinematics. *Geology*, *49*(2), 150–155. https://doi.org/10.1130/G47985.1

Stanca, R. M., Paton, D. A., Hodgson, D. M., McCarthy, D. J., & Mortimer, E. J. (2019). A revised position for the rotated Falkland Islands microplate. *Journal of the Geological Society*, *176*(3), 417–429. https://doi.org/10.1144/jgs2018-163

Steinberger, B., Bredow, E., Lebedev, S., Schaeffer, A., & Torsvik, T. H. (2019). Widespread volcanism in the Greenland–North Atlantic region explained by the Iceland plume. *Nature Geoscience*, *12*(1), 61–68. https://doi.org/10.1038/s41561-018-0251-0

Svartman Dias, A. E., Lavier, L. L., & Hayman, N. W. (2015). Conjugate rifted margins width and asymmetry: The interplay between lithospheric strength and thermomechanical processes. *Journal of Geophysical Research: Solid Earth*, *120*, 8672–8700. https://doi.org/doi:10.1002/2015JB012074

Szatmari, P., & Milani, E. J. (1999). Microplate rotation in northeast Brazil during South Atlantic rifting: Analogies with the Sinai microplate. *Geology*, *27*(12), 1115–1118. https://doi.org/10.1130/0091-7613(1999)027<1115:MRINBD>2.3.CO;2

Tentler, T. (2003). Analogue modeling of overlapping spreading centers: Insights into their propagation and coalescence. *Tectonophysics*, *376*(1–2), 99–115. https://doi.org/10.1016/j.tecto.2003.08.011

Tentler, T., & Acocella, V. (2010). How does the initial configuration of oceanic ridge segments affect their interaction ? Insights from analogue models, *115*. https://doi.org/10.1029/2008JB006269

Tetreault, J. L., & Buiter, S. J. H. (2018). The influence of extension rate and crustal rheology on the evolution of passive margins from rifting to break-up. *Tectonophysics*, *746*, 155–172. https://doi.org/10.1016/j.tecto.2017.08.029

Thatcher, W. (2007). Microplate model for the present-day deformation of Tibet. *Journal of Geophysical Research: Solid Earth*, *112*(1), 1–13. https://doi.org/10.1029/2005JB004244

Turcotte, D. L., & Schubert, G. (2002). *Geodynamics*. Cambridge University Press.

Vendeville, B., & Le Calvez, J. (1995). Physical models of normal-fault relays between variably offset grabens. *AAPG Bulletin*, *79*.

Watremez, L., Lau, K. H., Nedimovic, M. R., & Louden, K. E. (2015). Traveltime tomography of a dense wide-angle profile across Orphan Basin. *Geophysics*, *80(3)*, B69–B82.

Welford, J. K., Dehler, S. A., & Funck, T. (2020). Crustal velocity structure across the Orphan Basin and Orphan Knoll to the continent–ocean transition, offshore Newfoundland, Canada. *Geophysical Journal International*, *221*(1), 37–59. https://doi.org/10.1093/gji/ggz575

Welford, J. K., Shannon, P. M., O'Reilly, B. M., & Hall, J. (2012). Comparison of lithosphere structure across the Orphan Basin-Flemish Cap and Irish Atlantic conjugate continental margins from constrained 3D gravity inversions. *Journal of the Geological Society*, *169*(4),

405–420. https://doi.org/10.1144/0016-76492011-114

Wessel, P., Luis, J. F., Uieda, L., Scharroo, R., Wobbe, F., Smith, W. H. F., & Tian, D. (2019). The Generic Mapping Tools Version 6. *Geochemistry, Geophysics, Geosystems*, *20*(11), 5556–5564. https://doi.org/https://doi.org/10.1029/2019GC008515

Williams, H. (1984). Miogeoclines and suspect terranes of the Caledonian- Appalachian orogen: tectonic patterns in the North Atlantic region. *Canadian Journal of Earth Sciences*, *21*, 887–901.

Williams, H. (1995). Geology of the Appalachian-Caledonian orogen in Canada and Greenland. *Geological Survey of Canada, Geology of Canada*, *6*.

Yang, P., & Welford, J. K. (2021). Investigating the Porcupine Atlantic margin, offshore Ireland, through integration of new seismic reflection and gravity data. *Tectonophysics*, *807*, 228809. https://doi.org/10.1016/j.tecto.2021.228809

Zalán, P. V, Severino, M. do C. G., Rigoti, C. A., Magnavita, L. P., de Oliveira, J. A. B., & Vianna, A. R. (2011). An Entirely New 3D-View of the Crustal and Mantle Structure of a South Atlantic Passive Margin – Santos, Campos and Espírito Santo Basins, Brazil (p. Search and Discovery Article #30177). AAPG.

Zwaan, F., Schreurs, G., Naliboff, J., & Buiter, S. J. H. (2016). Insights into the effects of oblique extension on continental rift interaction from 3D analogue and numerical models. *Tectonophysics*, *693*, 239–260. https://doi.org/10.1016/j.tecto.2016.02.036

Supporting Information for

Formation of continental microplates through rift linkage: Numerical modelling and its application to the Flemish Cap and Sao Paulo Plateau

Derek Neuharth[1,2], Sascha Brune[1,2], Anne Glerum[1], Christian Heine[3], J. Kim Welford[4]

[1]GFZ German Research Centre for Geosciences, Telegrafenberg, 14473 Potsdam, Germany.

[2]Institute of Geosciences, University of Potsdam, Germany.

[3]Specialist Geosciences, PTD/E/F, Shell Global Solutions International B.V., Rijswijk, NL

[4]Department of Earth Sciences, Memorial University of Newfoundland, St. John's, Newfoundland, Canada

Contents of this file

Additional Supporting Information (Files uploaded separately)

Summary

In this supplementary material, we provide a table detailing model parameters as well as animations showcasing the evolution of the 1) oblique linkage (*Regime 1*, movie S1), 2) transform linkage (*Regime 2*, movie S2), 3) microplate formation (*Regime 3*, movie S3), and rift jump without microplate (*Regime 4*, movie S4) reference model evolutions discussed in the paper. We include 4 additional figures including an initial density profile (Fig. S1), a larger model domain (900x900 km, Fig. S2), and a regime diagram for varied lithosphere thickness and X-offset (Fig. S3). Additionally, we include two models with a mantle plume where we vary the plume placement from the left to right side of the model. In the text we describe the model setup shown in Fig. S4 and briefly cover the evolution of these models. Two additional animations showcase the evolution of these models (movies S5 and S6). All models were run using dealii version 9.1.1, and the ASPECT version with all model parameter files is found here: https://doi.org/10.5281/zenodo.4601188.

Text S1.

To test the effects the arrival of a mantle plume has on microplate development, we setup a model similar to the reference microplate setup with an X- and Y- offset of 300 km, and a

crustal strength ratio of 25 km upper crust to 10 km lower crust. The model depth is extended to 360 km and we place the plume center at 600 km in the X-direction and 300 km in the Y-direction. The plume is prescribed as a Gaussian function on the bottom boundary, where a maximum velocity (0.4 m/yr), temperature anomaly (300 K), and radius (200 km) determine the size, inflow, and temperature of the plume (Figure S1). The plume arrives in two phases: from 10-15 Myr plume inflow uses the above-mentioned parameters (plume head phase), with a volume flux of ~350 m^3/s. From 15 Myr until the end of the model run, the maximum velocity, temperature anomaly, and radius are halved to mimic the plume stem, which in this case has a volume flux of 43 m^3/s. The remainder of the bottom boundary is prescribed an inflow or outflow to conserve mass. To determine this value, we integrate the total inflow from the plume and subtract from this the outflow related to the side boundaries. Everywhere outside of the plume is given a velocity to balance the left-over flow.

In the first 10 Myr, both rift arms propagate into undeformed crust and curve inward where overlap occurs (supplementary video S5). This is followed by localization into the center of the rift valleys, leading to both rift arms having a ~225 km long orthogonal fault section with no overlap between the rifts, and ~170 km oblique sections with overlap. The plume head starts to rise through the model at 10 Myr and by 10.5 Myr has impinged on the lithosphere underneath the eastern rift arm. Plume material spreads to both sides, reaching the model boundary on the eastern side, and forming a channel of warm material flowing to the western rift on the other side. Both rifts migrate towards the boundaries. However, while the western rift has relatively symmetric spreading, the eastern rift migrates asymmetrically at a faster rate, leaving a thinned continental margin attached to the microplate. By 15 Myr, seafloor spreading has started at the northern boundary on the eastern rift. As asymmetric rift migration continues, the obliquity of the eastern rift's overlapping segment increases from ~45°at 15 Myr to ~60° at 21 Myr. Simultaneously, the center of rotation of the microplate migrates to the southwest until 21 Myr, at which time the eastern rift attaches to the southern boundary, and the western rift subsequently dies out.

To test the effect of plume position on model evolution, we ran a separate simulation initially placing the plume on the western side at 300 km in the X- and 300 km in the Y-direction (supplementary video S6). The model evolves similarly to the one with the eastern plume location, with the plume impinging and beginning to spread underneath the lithosphere by 10.5 Myr. In this case, plume material is more localized in the western rift, and extension occurs at a faster rate compared to the eastern rift. As extension continues, the western rift propagates across the model domain faster, but remains relatively orthogonal while the eastern rift increases in obliquity. The center of rotation migrates to the northeast until ~23.5 Myr, when the western rift attaches to the northern model boundary, causing the microplate to attach to the eastern side. The eastern rift completely dies out by 24.5 Myr. Although the evolution remains similar, model plume placement is therefore an important factor in determining which rift takes over, and the side the microplate attaches to.

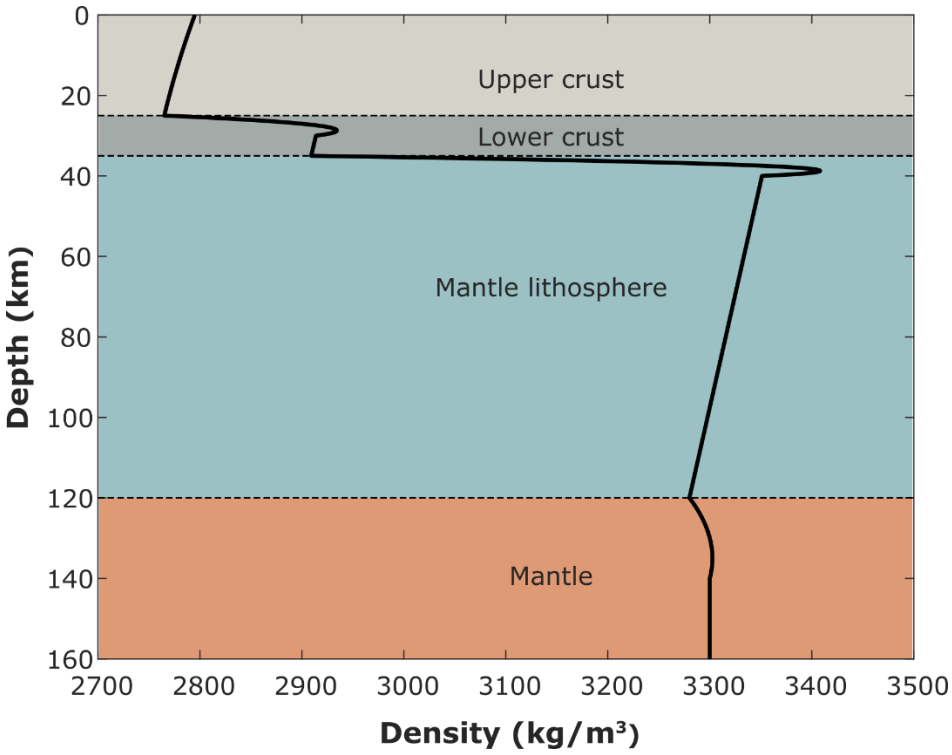

Figure S1. Initial density profile where colors indicate composition.

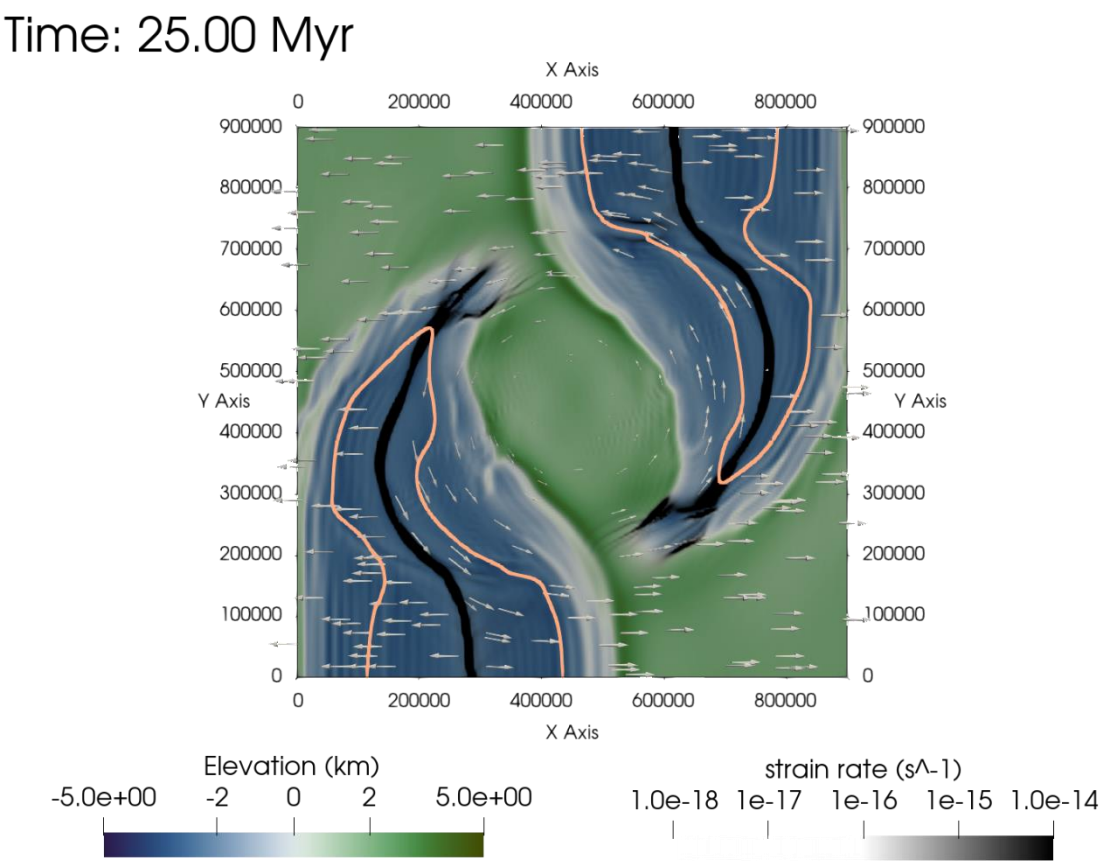

Figure S2. Example of larger 900x900 (X and Y) microplate model which was given an initial X-offset of 400 km, Y-offset of 300 km, crustal ratio of 25:10, and lithosphere thickness of 120 km (i.e. similar to models of Fig. 5 and 6h, but in a larger model domain). Orange line indicates the landward limit of oceanic crust.

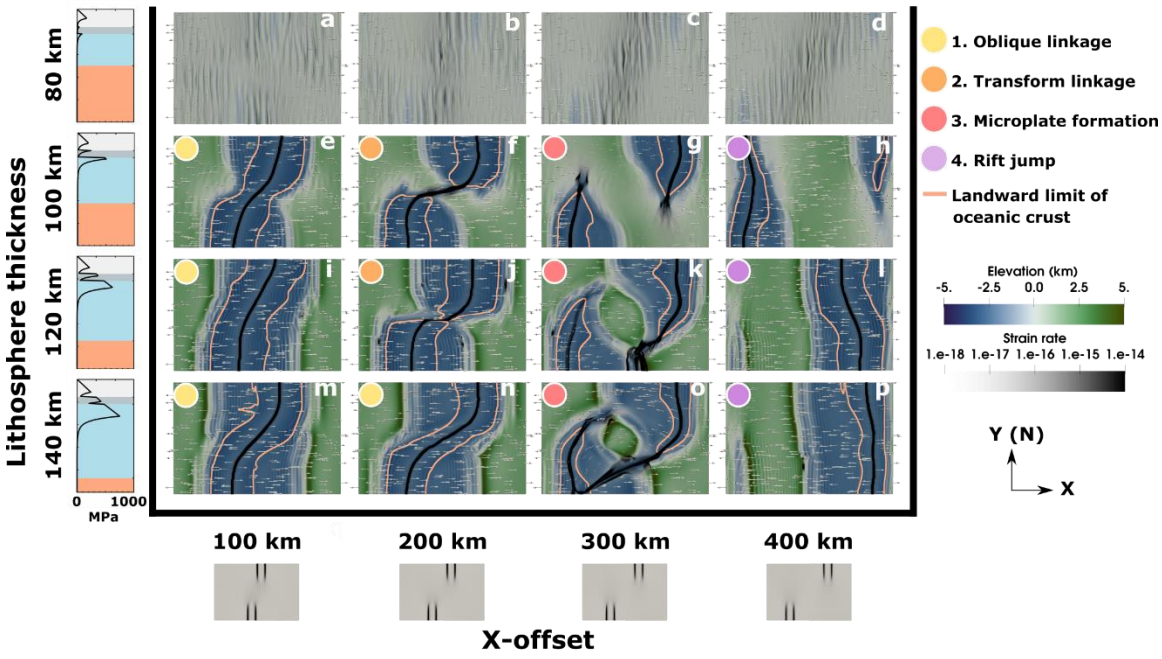

Figure S3. Regime diagram showing the types of rift connections when varying the lithosphere thickness, and the initial x- offset. Models are shown from a top down view at 25 Myr, and are colored by elevation and the strain rate, with the orange line representing the landward limit of oceanic crust (>70% asthenosphere material). On the left, strength envelopes are shown, with the compositions of upper (light gray) and lower (dark gray) crust, mantle lithosphere (blue), and mantle (orange). Models are divided into regimes shown with colored dots in the top-left corners of the model images.

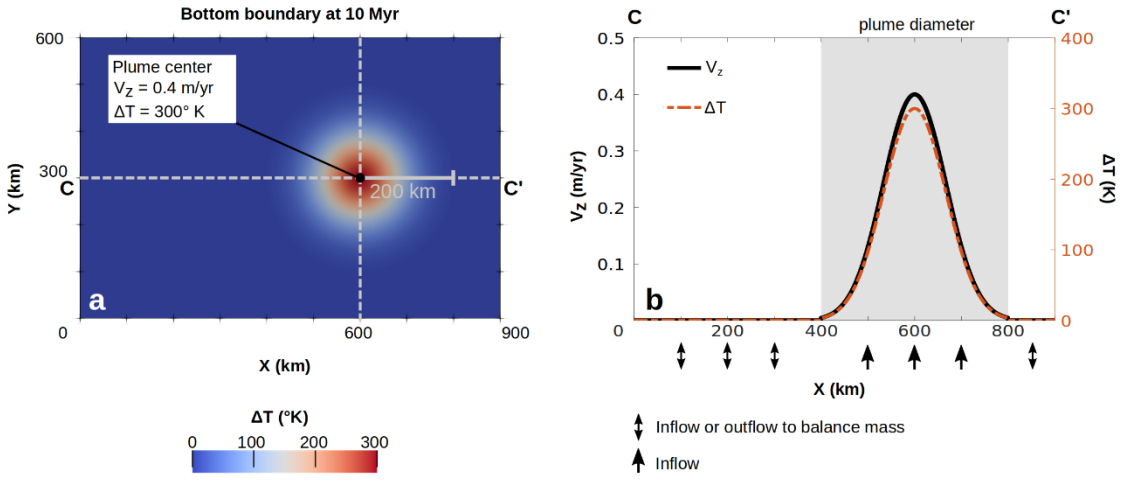

Figure S4. Setup for the rift model including a mantle plume. The setup shows the initial state of the plume head phase, which runs from 10 to 15 My. a) Top view of bottom boundary excess temperature $\boldsymbol{\Delta T}$ at 10 Myr when the plume is initially emplaced. b) Plume excess

temperature $\boldsymbol{\Delta T}$ (dashed red line) and the Z component of velocity $\boldsymbol{V_z}$(black line) along the transect CC′ in a. The gray box shades the area within the plume radius.

Parameter	Symbol	Units	Upper crust	Lower crust	Lithospheric mantle	Asthenosphere
Reference density	ρ_0	kg m^{-3}	2700	2850	3280	3300
Thermal expansivity	α	K^{-1}	$2.7{\cdot}10^{-5}$	$2.7{\cdot}10^{-5}$	$3.0{\cdot}10^{-5}$	$3.0{\cdot}10^{-5}$
Thermal diffusivity	κ	m^2 s^{-1}	$7.72{\cdot}10^{-5}$	$7.31{\cdot}10^{-5}$	$8.38{\cdot}10^{-7}$	$8.33{\cdot}10^{-7}$
Heat capacity	C_p	J kg^{-1} K^{-1}	1200	1200	1200	1200
Heat production	H	W m^{-3}	$0.7{\cdot}10^{-6}$	$0.2{\cdot}10^{-6}$	0	0
Cohesion	C	Pa	$5{\cdot}10^{6}$	$5{\cdot}10^{6}$	$5{\cdot}10^{6}$	$5{\cdot}10^{6}$
Internal friction angle (unweakened)	ϕ	°	26.56	26.56	26.56	26.56
Strain weakening interval	-	-	[0,1]	[0,1]	[0,1]	[0,1]
Strain weakening factor	ϕ_{wf}	-	0.1	0.1	0.1	0.1
Creep properties			***Wet quartzite***	***Wet anorthite***	***Dry olivine***	***Dry olivine***
Stress exponent (dis)	n	-	4.0	3.0	3.5	3.5
Constant prefactor (dis)	A_{dis}	Pa^{-n} s^{-1}	$8.57{\cdot}10^{-28}$	$7.13{\cdot}10^{-18}$	$6.52{\cdot}10^{-16}$	$6.52{\cdot}10^{-16}$
Activation energy (dis)	E_{dis}	J mol^{-1}	$223{\cdot}10^{3}$	$345{\cdot}10^{3}$	$530{\cdot}10^{3}$	$530{\cdot}10^{3}$
Activation volume (dis)	V_{dis}	m^3 mol^{-1}	0	$38{\cdot}10^{-6}$	$18{\cdot}10^{-6}$	$18{\cdot}10^{-6}$
Constant prefactor (diff)	A_{diff}	Pa^{-1} s^{-1}	$5.79{\cdot}10^{-19}$	$2.99{\cdot}10^{-25}$	$2.25{\cdot}10^{-9}$	$2.25{\cdot}10^{-9}$
Activation energy (diff)	E_{diff}	J mol^{-1}	$223{\cdot}10^{3}$	$159{\cdot}10^{3}$	$375{\cdot}10^{3}$	$375{\cdot}10^{3}$
Activation volume (diff)	V_{diff}	m^3 mol^{-1}	0	$38{\cdot}10^{-6}$	$6{\cdot}10^{-6}$	$6{\cdot}10^{-6}$
Grain size (diff)	d	m	0.001	0.001	0.001	0.001
Grain size exponent (diff)	m	-	2.0	3.0	0	0

Table S1. Reference parameter values. dis – dislocation creep. diff – diffusion creep.

Movie S1. Animation showing the evolution of the reference regime 1 model (Fig. 2), with an X- offset of 100 km and Y- offset of 300 km. The upper portion shows a top-down view of the model colored by elevation (blue to green) and strain rate (black), with arrows indicating horizontal velocity magnitude and direction and orange contours to show the landward limit of oceanic crust. The bottom portion shows a slice along profile A to A′, with layers colored to show the upper crust (white), lower crust (gray), lithospheric mantle (blue), and the mantle (blue).

Movie S2. Animation showing the evolution of the reference regime 2 model (Fig. 3), with an X- offset of 100 km and Y- offset of 300 km. The upper portion shows a top-down view of the

model colored by elevation (blue to green) and strain rate (black), with arrows indicating horizontal velocity magnitude and direction and orange contours to show the landward limit of oceanic crust. The bottom portion shows a slice along profile A to A', with layers colored to show the upper crust (white), lower crust (gray), lithospheric mantle (blue), and the mantle (blue).

Movie S3. Animation showing the evolution of the reference regime 3 model (Fig. 4), with an X- offset of 300 km and Y- offset of 300 km. The upper portion shows a top-down view of the model colored by elevation (blue to green) and strain rate (black), with arrows indicating horizontal velocity magnitude and direction and orange contours to show the landward limit of oceanic crust. The bottom portion shows a slice along profile A to A', with layers colored to show the upper crust (white), lower crust (gray), lithospheric mantle (blue), and the mantle (blue).

Movie S4. Animation showing the evolution of the reference regime 4 model (Fig. 5), with an X- offset of 400 km and Y- offset of 300 km. The upper portion shows a top-down view of the model colored by elevation (blue to green) and strain rate (black), with arrows indicating horizontal velocity magnitude and direction and orange contours to show the landward limit of oceanic crust. The bottom portion shows a slice along profile A to A', with layers colored to show the upper crust (white), lower crust (gray), lithospheric mantle (blue), and the mantle (blue).

Movie S5. Animation showing the evolution of a microplate model where a plume impinges on the right side of the model domain at 10 Myr. The upper portion shows a top-down view of the model colored by elevation (blue to green) and strain rate (black), with arrows indicating horizontal velocity magnitude and direction and orange contours to show the landward limit of oceanic crust. The bottom portion shows a slice along profile A to A', with layers colored to show the upper crust (white), lower crust (gray), lithospheric mantle (blue), and the mantle (blue). Unlabeled temperature contours show temperatures of 1400, 1450, 1500, 1550, and 1600 °C.

Movie S6. Animation showing the evolution of a microplate model where a plume impinges on the left side of the model domain at 10 Myr. The upper portion shows a top-down view of the model colored by elevation (blue to green) and strain rate (black), with arrows indicating horizontal velocity magnitude and direction and orange contours to show the landward limit of oceanic crust. The bottom shows a slice along profile A to A', with layers colored to show the upper crust (white), lower crust (gray), lithospheric mantle (blue), and the mantle (blue). Unlabeled temperature contours show temperatures of 1400, 1450, 1500, 1550, and 1600 °C.